



Annual cycle of surface-coupling effects on Arctic mixed-phase clouds during MOSAiC

Hannes J. Griesche¹, Ronny Engelmann¹, Martin Radenz¹, Julian Hofer¹, Dietrich Althausen¹, Albert Ansmann¹, Kevin Barry², Jessie Creamean², Cristofer Jimenez¹, and Patric Seifert¹

¹Remote Sensing of Atmospheric Processes, Leibniz Institute for Tropospheric Research, Leipzig, Germany

²Department of Atmospheric Science, Colorado State University, 1371 Campus Delivery, Fort Collins, Colorado, 80523-1371, United States of America

Correspondence: Hannes J. Griesche (griesche@tropos.de)

Abstract. Persistent mixed-phase clouds frequently occurred in the Arctic and have significant impacts on the Arctic climate. The surface mixed-layer (SML) coupling status of these clouds impacts their microphysical properties. During a Arctic summer cruise in 2017, surface-coupled clouds were observed to contain ice more often than decoupled clouds at low-supercooling temperatures. Here, an annual cycle of Arctic mixed-phase cloud ice-formation temperatures is presented for the Arctic ice-drift experiment Multidisciplinary drifting Observatory for the Study of Arctic Climate (MOSAiC) in 2019 and 2020. From October until March no clouds with cloud minimum temperatures above -10°C were observed. From April to September an increased fraction of ice-containing clouds was observed for clouds with minimum temperatures between -7.5°C and -5°C (between 40% and 70%). Between April and July SML-coupled clouds with a minimum temperature above -7.5°C showed an enhanced fraction of ice-containing clouds, compared to decoupled clouds (2 – 3 times higher). Also, SML-coupled clouds were 2 – 4 times more likely to be observed during this period. In August + September the ratio of coupled-to-decoupled ice-containing clouds reduced to 1.3, due to a higher frequency of occurrence of ice-containing decoupled clouds. Using surface-based ice-nucleating particle (INP) measurements the observed phenomena could likely be attributed to the presence of INPs active above -15°C at the surface. Analysis of sea-ice concentration in the surrounding region, the distance to the ice edge, and the travel time along the back-trajectories to the marginal ice zone supports this finding.

1 Introduction

Ice formation in mixed-phase clouds, clouds which consist of liquid-droplets and ice-crystals at the same time, plays a critical role in the complex processes which are modulating the cloud properties, precipitation processes, their radiative effect, and cloud lifetime (Morrison et al., 2012). The phase partitioning in mixed-phase clouds is closely interlinked with turbulence, the humidity supply, and the availability of cloud-relevant aerosol particles, such as ice-nucleating particles (INP) and cloud condensation nuclei (CCN) (Morrison et al., 2012; Kalesse et al., 2016; Radenz et al., 2021). The transition of liquid water or water vapor to ice (or vice versa) can change the cloud properties dramatically, as for example the cloud radiative effect, which is dominated by the liquid phase of the cloud (Shupe et al., 2004). Ice formation in clouds in the so-called heterogeneous temperature regime, i.e., approximately down to -38°C , is initiated by an INP (Hoose and Möhler, 2012), a rare subset of all



aerosol particles in the atmosphere. If both cloud phases, liquid and ice, are present in the same volume, ice crystals will grow on the expense of the liquid water according to the Wegener-Bergeron-Findeisen process (Wegener, 1912; Bergeron, 1935; Findeisen, 1938). Jimenez et al. (2025) showed that ice formation in free-tropospheric Arctic mixed-phase clouds is dominated by immersion freezing, a freezing process where the ice formation is triggered by an INP, which is already immersed into the droplet reaching its activation temperature. Due to the persistent droplet formation, the authors concluded that the free Arctic tropospheric CCN and INP reservoir is unlikely to be depleted, and the dissipation of the observed clouds was rather due to insufficient water vapor supply.

Riming, ice-crystal and liquid-droplet collision, as well as aggregation, ice-crystal and ice-crystal collision, are two major contributors to the ice mass in Arctic mixed-phase clouds (Chellini et al., 2022; Maherndl et al., 2024). Using ground-based remote sensing of clouds at Ny-Ålesund, Svalbard, Chellini and Kneifel (2024) identified turbulence as a relevant factor for aggregation and riming of ice particles between -20°C and -10°C and argued that this also increases secondary ice production (SIP). SIP has been shown to play a substantial role in Arctic mixed-phase clouds by tethered-balloon borne observations made in Svalbard (Pasquier et al., 2022). Radenz et al. (2021) showed that gravity waves forced by the orography along the trajectory of the air mass, influence the ice occurrence at temperatures below -15°C . The occurrence of low-level clouds in the Arctic typically increases during spring time, which was, based on space-borne lidar observations, attributed to an enhanced fraction of liquid-containing mixed-phase clouds on the expense of pure-ice clouds (Lac et al., 2025). Yet, certain aspects of some underlying mechanisms controlling Arctic mixed-phase clouds are still under discussion and models struggle, for example, to reproduce the observed cloud annual cycle, the relative distribution of liquid and ice, especially in low-level clouds, (Taylor et al., 2019; Wei et al., 2021; Shaw et al., 2022), and the role of aerosol particles in Arctic cloud processes (Schmale et al., 2021; Kiszler et al., 2024).

INPs of different composition trigger ice formation at different temperatures. Dust particles are globally one of the most prominent INPs below -15°C (Ansmann et al., 2009; Seifert et al., 2010; Murray et al., 2012; Kanji et al., 2017; Villanueva et al., 2025), and can enter the Arctic via long-range transport (Si et al., 2019). Above -15°C , ice formation is usually associated with INPs containing biogenic material (Pereira Freitas et al., 2023; Hartmann et al., 2025). In the Arctic, such INPs can either originate from local sources, such as sea spray aerosol, local dust emissions, e.g., from glacial outwash, and local primary biological activity, or the respective particles were advected into the Arctic via long-range transport (DeMott et al., 2016; Šantl Temkiv et al., 2019; Tobo et al., 2019; Creamean et al., 2020; Ansmann et al., 2023; Wieber et al., 2025). Highly active INPs have been found close to melting sea ice and in melt water samples (Wilson et al., 2015; Irish et al., 2017; Zeppenfeld et al., 2019; Mavis et al., 2025), in airborne samples collected over polynyas (Hartmann et al., 2020), as well as close to the North Pole (Porter et al., 2022). Creamean et al. (2022) presented the annual cycle of surface INP concentrations in the high Arctic ocean from the Multidisciplinary drifting Observatory for the Study of Arctic Climate (MOSAIC) expedition and highlighted a maximum of INPs active above -15°C during summer. During winter and spring, the dominating INP sources were long-range transport, while during the melt season in summer biogenic particles likely from local sources prevailed. Still, biogenic material was found in the INP samples throughout the whole year (Barry et al., 2025). Based on ship-based lidar observations made during MOSAiC, Ansmann et al. (2023) presented an annual cycle of aerosol optical properties and CCN



and INP concentrations in the boundary layer and the free troposphere. The INP concentrations were higher during summer and a shift of the dominating ice-forming particle type from dust particles in winter to sea spray aerosol in summer was identified. However, the distribution of local terrestrial and marine aerosol sources and their contribution to the INP availability, are still under discussion (Creamean et al., 2018; Wex et al., 2019; Hartmann et al., 2021; Schmale et al., 2021).

A significant feature of Arctic mixed-phase clouds is the formation of a shallow liquid-dominated layer at cloud top. This layer introduces convection in the cloud due to strong radiative cooling at the top (Shupe et al., 2008; Egerer et al., 2019; Lonardi et al., 2022), which can cause an exchange of the cloud with a mixed-layer below cloud base (Brooks et al., 2017). The depth of such a convective mixed-layer is correlated to cloud properties, such as liquid water path and cloud top height (Shupe et al., 2013). If this cloud mixed-layer (CML) reaches the turbulent surface mixed-layer (SML), surface properties can influence the cloud properties by serving as source for moisture but also for cloud relevant aerosol particles (Eirund et al., 2019; Gierens et al., 2020; Griesche et al., 2021; Radenz et al., 2021). Using radiosonde and tethered ballon profiles Akansu et al. (2023) showed that under cloudy conditions the SML usually is higher, compared to cloudless conditions. The CML and the SML together are denoted here as planetary boundary layer (PBL), which is capped by a temperature inversion, usually at cloud top (Brooks et al., 2017). Above Arctic mixed-phase clouds specific humidity inversions were regularly observed, which can serve as additional resupply for moisture via cloud top entrainment (Sedlar et al., 2012; Neggers et al., 2019; Egerer et al., 2021). Also, cloud relevant particles in the free troposphere, e.g., from long-range transport can be entrained downward into the PBL (Igel et al., 2017; Solomon et al., 2018).

Substantial research has been conducted on the influence of the coupling between the CML and SML on mixed-phase cloud properties. Creamean et al. (2021) used tethered balloon observations to investigate the vertical aerosol distribution in the Arctic PBL. The authors found, that only in 14% of the analyzed profiles, the aerosol particles were uniformly mixed between the surface and the cloud base. Using ground-based remote sensing at the Arctic site Ny-Ålesund, Svalbard, Gierens et al. (2020) showed that cloud coupling to the SML has an influence on the cloud properties. Under coupled situations, for example, they observed clouds with enhanced liquid water path (LWP), compared to decoupled situations. Clouds coupled to the water vapor transport (WVT) from sea ice leads in the central Arctic have been found to show a larger liquid fraction, lower cloud base, and a larger vertical extend, compared to clouds decoupled from the WVT (Saavedra Garfias et al., 2023). For two different pre-Alpine sites, Ohneiser et al. (2025a) showed that the resupply of INPs from the free troposphere may also be limited due to the stability at the top of the PBL. The authors analyzed INP filter samples from Hohenpeißenberg, Germany, and Eriswil, Switzerland, during northeasterly winds, which caused a situation with comparable air masses probed at both sites. INP spectra from filters taken with a temporal lag of 12 hours between both sites revealed a higher fraction of INPs active above -15°C at Hohenpeißenberg, when Hohenpeißenberg was, due to its higher altitude, located in the free troposphere, while Eriswil was in the PBL. Jozef et al. (2024) analyzed seasonal patterns in the tropospheric stability during MOSAiC based on radiosonde profiles. The authors found stronger stability during winter and spring and least stability during fall. During summer they found similar occurrences of both cases, strong stability and weak stability. The authors hypothesized that a stronger stability may lead to more decoupled cases, while a weaker stability supports SML-coupling. Based on 10 years of satellite remote sensing Papakonstantinou-Presvelou et al. (2022) found an increased ice-crystal number concentration in



clouds that have been observed over the Arctic sea-ice, compared to clouds above the open ocean. Above both surface types
 95 the ice-crystal numbers were increased, when only coupled clouds were considered. Griesche et al. (2021) analyzed ship-
 based remote sensing of clouds and aerosol particles from a two month expedition in the high Arctic. The authors found that
 clouds, which were thermodynamically coupled to the surface, contained ice more frequently, compared to decoupled clouds,
 especially at temperatures above -15°C . They argued that this phenomenon is likely due to a local source of INPs containing
 biogenic material, which were transported into the clouds, if the clouds were coupled to the surface. Such biogenic material
 100 can include, among others, polysaccharides and proteins emitted from the ocean. Marine polysaccharides, in particular, have
 recently been shown to act as efficient ice-nucleating molecules (Hartmann et al., 2025) and to reach high altitudes up to the
 free troposphere, as demonstrated by a recent balloon study in Ny-Ålesund (Zeppenfeld et al., 2025).

The presented study is a follow up of Griesche et al. (2021), using an entire year of observations in the Arctic ocean. We use
 data from the year-long Arctic ice-drift expedition MOSAiC (Shupe et al., 2022). The MOSAiC expedition took place from
 105 September 2019 until October 2020 and aimed to observe a full annual cycle of the Arctic system. MOSAiC was based on the
 German icebreaker Polarstern, which was located in the central Arctic for the whole period, except for a small interruption
 end of May until beginning of June 2020, where the sea-ice was left for a crew rotation. The track of the MOSAiC expedition
 is depicted in Fig. 1. Continuous ground-based remote sensing from cloud radar and lidar was used to identify clouds and
 classify their phase and vertical extent (Engelmann et al., 2021; Shupe et al., 2022; Griesche et al., 2024b). By means of
 110 radiosonde profiles, the liquid-dominated layer base derived from the lidar observations, and the cloud top from the cloud radar
 the SML-coupling state of the cloud and the cloud-minimum temperature were derived. Additionally, in situ observations of
 INPs, HYSPLIT back-trajectory analyses, and sea-ice concentration from satellite observations were used to constrain links
 between the coupling-state of the cloud and surface properties.

The article is structured as follows. Section 2 gives an overview of the used instruments and observations. In Section 3 the
 115 applied methodology is introduced. The determination of the relevant cloud properties, such as phase, liquid-dominated layer
 base and cloud top, cloud minimum temperature, and coupling state is presented. Additionally, the utilization of the supporting
 information from datasets such as INP filters, trajectories, and sea-ice concentration is introduced. The results are presented in
 Section 4 and discussed in Section 5. Final conclusions are given in Section 6.

2 Instrumentation

120 Ground-based remote sensing was performed from aboard Polarstern by means of different platforms during the entire MO-
 SAiC year. One of the remote-sensing sites operated during MOSAiC was the OCEANET-Atmosphere (hereafter referred to as
 OCEANET) container from the Leibniz-Institute for Tropospheric Research TROPOS, Leipzig, Germany (Engelmann et al.,
 2021; Griesche et al., 2024b). The mobile platform OCEANET has previously been operated on different research vessels and
 earlier voyages (Kanitz et al., 2013; Bohlmann et al., 2018; Griesche et al., 2020), and based for one year in Antarctica at the
 125 German Neumayer Station III (Radenz et al., 2024).

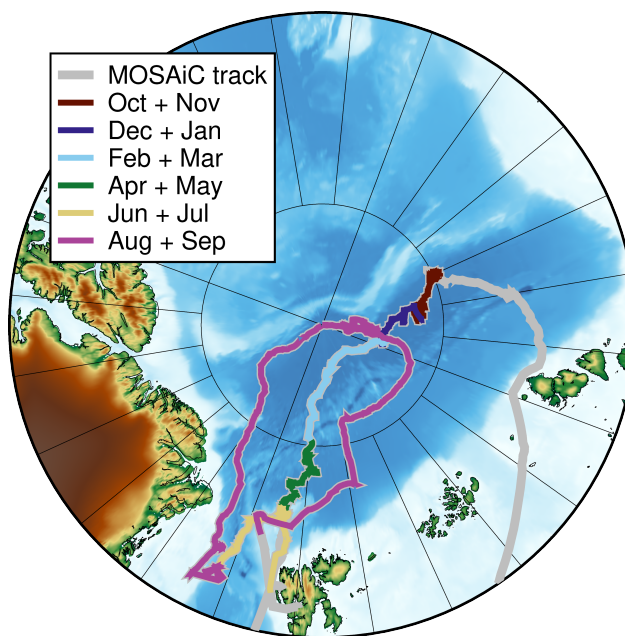


Figure 1. Track during the MOSAiC expedition (grey line). The different colored lines shows the part of the track Polarstern drifted during each two-month period analyzed in Fig. 4. The map was created with PyGMT (Tian et al., 2023).

During MOSAiC, OCEANET comprised a multiwavelength depolarization Raman lidar Polly^{XT}, two microwave radiometers, two disdrometers, as well as a terrestrial and a solar radiation sensor. The Polly^{XT} emits light at 355 nm, 532 nm, and 1064 nm and has far range receiver channels for the elastic backscattered light at 355 nm, 532 nm, and 1064 nm with a complete overlap in 700 m (Engelmann et al., 2016). Additional near range receiver for elastic-backscatter are implemented at 130 355 nm and 532 nm with a complete overlap in 120 m. Raman-scattered light was measured at 387 nm, 407 nm, and 607 nm for nitrogen and water vapor information (Seidel et al., 2025). Finally, depolarization information was retrieved at 355 nm and 532 nm. The measurement from Polly^{XT} were averaged to 30 s profiles with a vertical resolution of 7.5 m.

Another remote-sensing site operated during the MOSAiC expedition was the Atmospheric Radiation Measurement (ARM) mobile facility 2 (AMF2) from the United States (US) Department of Energy. The AMF2 was equipped with, among others, 135 different lidar and cloud radar systems, and a wind profiler. For this study the Ka-band ARM Zenith cloud radar (KAZR) was utilized, which operates at 35 GHz. The KAZR was operated with a temporal resolution of 2 s and a vertical resolution of 30 m. Besides remote sensing, in situ measurements were also performed on the AMF2 platform. A filter sampler was installed roughly at 15 m above sea level for INP sampling. INP filters were changed every 3 days and analyzed off-line subsequent to the expedition at Colorado State University (CSU), US (Barry et al., 2025).

140 In situ profiles of thermodynamic state of the whole tropospheric column were derived by radiosonde launches, which were performed at least every 6 hours during the entire year. These profiles provide atmospheric pressure, humidity and temperature.



Table 1. Applied instruments and their specifications. ν represents the respective applied frequency of the instrument and λ the wavelength. R indicates the measurement range and P the precision of the measured quantity. T specifies the respective temporal resolution and V the vertical resolution

Instrument Type (instrument reference) Platform	Used quantity (dataset reference)	Parameters and units	Resolution
<u>Raman Lidar</u> Polly ^{XT} (Engelmann et al., 2016) <i>OCEANET</i>	Attenuated backscatter (Engelmann et al., 2025)	$\lambda = 355, 532, 1064 \text{ nm}$ R: $0.1 - 20 \text{ km}, 0 - 1 \text{ km}^{-1} \text{ sr}^{-1}$ P: $10^{-5} \text{ km}^{-1} \text{ sr}^{-1}$	T: 30 s V: 7.5 m
	Volume depolarization ratio (Engelmann et al., 2025)	$\lambda = 355, 532 \text{ nm}$ R: $0.1 - 20 \text{ km}, 0 - 0.5$ P: 0.01	
<u>Doppler cloud radar</u> KAZR (Kollias et al., 2016) <i>AMF2</i>	Radar reflectivity factor (Lindenmaier et al., 2024)	$\nu = 35.5 \text{ GHz}$ R: $0.18 - 18 \text{ km}; -55 - 20 \text{ dBZ}$ P: 2 dBZ	T: 2 s V: 30 m
<u>Ice Spectrometer</u> off-line (Creamean et al., 2025) <i>AMF2</i>	INP concentration (Hill et al., 2024)	R: $-27 - 0 \text{ }^{\circ}\text{C}$ P: $0.5 - 1 \text{ }^{\circ}\text{C}$	T: 3 days
<u>Radiosonde</u> RS41 (Jensen et al., 2016) <i>Polarstern helideck</i>	Atmospheric pressure (Dahlke et al., 2023)	R: surface to 3 hPa P: 1 hPa ($> 100 \text{ hPa}$),	T: 1 s (launch at least every 6 hours)
	Atmospheric humidity (Dahlke et al., 2023)	R: $0 - 100 \%$ P: 4 %	V: $5 \text{ m at } 5 \text{ m s}^{-1}$ ascend speed
	Atmospheric temperature (Dahlke et al., 2023)	R: $-90 - 60 \text{ }^{\circ}\text{C}$ P: $0.3 \text{ }^{\circ}\text{C} (< 16 \text{ km})$	

Table 1 lists all the relevant instruments utilized in this study, their platforms, the utilized quantities, and the respective temporal and vertical resolution.

The combined remote-sensing dataset was, for example, used to derive continuous, height-resolved cloud microphysical cloud properties for the entire MOSAiC year (Engelmann et al., 2025), as described in Griesche et al. (2024a), based on the synergistic instrument approach of Cloudnet (Illingworth et al., 2007; Tukiainen et al., 2020). This dataset contains, among others, a pixel-based Cloudnet target classification of the cloud phase.



Table 2. Summary of the approaches and thresholds for cloud property identification.

Cloud property	Criterion	Constrain
Liquid-dominated layer base	$\beta_{nr,liquid\ base} / \beta_{nr,liquid\ layer\ max} \geq 0.06$ $\beta_{nr,liquid\ base+250\ m} / \beta_{nr,liquid\ base} = 0.15$ $\delta_{liquid\ base} \leq 0.03$	$\beta_{nr,liquid\ layer\ max} \geq 1 \cdot 10^{-5} \text{ sr}^{-1} \text{ mM}^{-1}$ $h_{liquid\ base} \geq 120 \text{ m}$
	β_{fr} $\beta_{fr,liquid\ base} / \beta_{fr,liquid\ layer\ max} \geq 0.06$ $\beta_{fr,liquid\ base+250\ m} / \beta_{fr,liquid\ base} = 0.15$ $\delta_{liquid\ base} \leq 0.03$	No liquid layer detected using β_{nr} $\beta_{fr,liquid\ layer\ max} \geq 1 \cdot 10^{-5} \text{ sr}^{-1} \text{ mM}^{-1}$ $h_{liquid\ base} \geq 120 \text{ m}$
Ice identification	$\delta \geq 0.03$	4 consecutive height bins Liquid-dominated layer identified
Cloud top height	Z	Connected to liquid layer base height Gap of 3 cloud radar range gates allowed Liquid-dominated layer identified
Cloud minimum temperature	Minimum T	Between liquid layer base and cloud top Maximum time difference 6 hours Liquid-dominated layer identified
Decoupling height	$h([\text{cumulative mean}\{\Theta_h\} - \Theta_h]) \geq 0.5 \text{ K}$	Maximum time difference 6 hours Liquid-dominated layer identified
Coupled state	Liquid layer base height \leq decoupling height	Decoupling height determined

3 Methodology

To study the influence of cloud SML-coupling on the ice occurrence likelihood, a stepwise analysis of the data was performed. Initially, the remote-sensing data was checked for a liquid-dominated layer base. In case of a detected liquid-dominated layer base, the corresponding cloud phase (liquid-only or ice-containing), cloud top height, and cloud minimum temperature were determined, and, finally, the respective SML-coupling state (coupled or decoupled) was identified. The whole analysis was done on data averaged to the 30 s resolution of the lidar data. The respective procedure is introduced in detail in the following and all criteria and constraints are summarized in Tab. 2.

The observations were analyzed for two months each, starting from October 2019 until end of September 2020, in order to retrieve sufficient statistics of the fraction of ice-containing clouds during the MOSAiC year. In Fig. 1 the respective parts of the MOSAiC expedition track for each two-month period are highlighted in different colors. Finally, sea-ice and back-trajectory analyses were done.



3.1 Liquid identification and cloud ice detection

160 The lidar is, due to its rather short wavelength in or near the visible range, in opposite to a cloud radar, more sensitive to the number of particles than to their sizes. Hence, the identification of a liquid-dominated layer was done by means of the normalized lidar attenuated backscatter β , following Jimenez et al. (2020). At each time step a liquid-containing cloud was identified if the respective attenuated backscatter profile normalized by its maximum $\beta_{\text{norm}} = \beta / \beta_{\text{max}}$ was greater than $\beta_{\text{norm,max}} = 0.06$. As in Jimenez et al. (2020), a 5-bin smoothing was applied to minimize the effect of signal noise on the detection algorithm.

165 This approach was developed for clouds in the free troposphere higher than 500 m, while this study focuses on low-level, SML-coupled clouds. Hence, additional constraining criteria were applied to the liquid-layer detection. The volume depolarization δ and β profiles were used, to, e.g., avoid a misclassification of backscatter signals corresponding to ice precipitation from low-level clouds as a liquid-containing layer. For a liquid-containing cloud identification, δ should therefore not exceed a value of 0.03. The additional criteria for the attenuated backscatter profile were as follows: The maximum of the attenuated backscatter β_{max} should exceed a value of $1 \cdot 10^{-5} \text{ sr}^{-1} \text{ mM}^{-1}$ and the signal should decrease by at least 85% within 250 m above the liquid-containing layer due to the strong attenuation by the droplets. Finally, only liquid-dominated layer base heights higher than 120 m were considered in the analysis, to account for the impact of the optical overlap of the lidar system on the signal profiles. The introduced liquid-layer detection approach was first applied to the near range channel of the Polly^{XT} system. If no liquid-containing layer was found in the near range data, the far range signal was analyzed.

170

175 The cloud phase determination was done by means of the lidar, though the cloud radar is actually more sensitive to ice particles. However, the cloud radar has its lowest usable range gate in 180 m above the instrument. To account for the frequently occurring low-level clouds in the Arctic the lidar volume depolarization ratio δ was used for ice detection. Ice was identified if δ exceeded a threshold $\delta_{\text{ice}} = 0.03$. δ_{ice} was theoretically derived in Griesche et al. (2021) by considering the lowest detectable ice water content from a lidar of $10^{-6} \text{ kg m}^{-3}$ (Bühl et al., 2016). Each depolarization ratio profile was screened for $\delta \geq \delta_{\text{ice}}$.

180 For an ice-containing cloud, the depolarization ratio profile should cross δ_{ice} for at least 4 consecutive lidar height bins (= 30 m) below the liquid layer base.

3.2 Cloud top and minimum temperature, and surface mixed-layer coupling

The cloud top height was derived by means of the cloud radar reflectivity Z . Starting from the liquid-dominated layer base height, Z was checked at each cloud radar range gate. The cloud top was set to the highest altitude, where Z was continuously connected to the liquid-dominated layer base. To account for small inhomogeneities in the clouds, a gap of 3 cloud radar range gates (= 90 m) was allowed. The cloud minimum temperature was set to the lowest temperature between liquid-dominated base and cloud top derived from the temporal closest radiosonde profile. The maximum time difference between the radiosonde and the cloud profile was set to 6 hours.

185

The SML-coupling was derived following Gierens et al. (2020), using the potential temperature Θ derived from measurements of the temporally closest radiosonde. The height where the difference between the cumulative mean of Θ and Θ exceeded 0.5 was set as the respective decoupling height. If the decoupling height was below the liquid-dominated base, the cloud was

190



considered as decoupled. A quasi constant Θ profile until cloud base and hence a decoupling height above the liquid-dominated base was classified as coupled. Same as for the cloud minimum temperature, only cases within 6 hours before or after a radiosonde launch were considered.

195 3.3 Fraction of ice-containing clouds

For each two-months period between October 2019 and September 2020, the clouds were categorized by their cloud minimum temperature in different temperature intervals. These intervals were separated at $T = [-40, -35, -30, -25, -20, -15, -10, -7.5, -5, -2.5, 0]^\circ\text{C}$. For the entire MOSAiC period, this analysis was done for all clouds. For the late spring and summer months, i.e., for April + May, June + July, and August + September, the clouds were additionally analyzed separated by their
 200 coupling state.

3.4 INP concentration, trajectories, and surface properties

Surface-based INP filter measurements from CSU (Hill et al., 2024) were used to investigate a possible connection between elevated INP concentrations at the ground and ice formation in the clouds. INP filter collection and analysis is described in detail by Barry et al. (2025) but is briefly detailed here. Filters were prepared and collected following ultraclean procedures to
 205 ensure sample integrity as described by Barry et al. (2021). During MOSAiC, the sampling setup included a totalizing mass flow meter, vacuum pump, tubing, and precipitation shield. Filters were typically collected for 72 hours, totaling to an average of 88,000 sL (standard liters) of air per filter. After collection, filters were stored and shipped frozen until analysis at CSU.

For analysis, the CSU Ice Spectrometer (IS) was used (e.g., Creamean et al., 2025). Particles were re-suspended from filters into 7 – 10 mL of 0.1 μm -filtered deionized water in sterile 50 mL tubes and rotated for 20 min to ensure mixing. Each IS
 210 consists of two 96-well aluminum blocks encased by cold plates, with two instruments run in parallel. Aliquots of 50 μL were dispensed into four sterile 96-well polymerase chain reaction (PCR) plates using up to five 11 – 15-fold serial dilutions. Plates were sealed in the IS, purged with HEPA-filtered N_2 , and cooled at $0.33^\circ\text{C min}^{-1}$ while freezing is recorded every 0.5°C . The detection limit ranged from -27°C to -29°C depending on the deionized water blanks. INP number concentrations were calculated following Vali (1971) from the fraction of frozen droplets, volume of sample suspension, and total air volume
 215 filtered.

Back-trajectories were calculated using the transport and dispersion model HYSPLIT (Stein et al., 2015). 10-days trajectories were derived, initialized every hour at the liquid layer base of each analyzed cloud. These trajectories were, for example, used to calculated the time the sampled air parcels needed to travel from the ice edge to the measurement site.

To investigate the influence of different surface properties, the sea ice concentration (SIC), and the lead and melt-pond
 220 fraction were analyzed. The SIC was derived from the satellite-based merged MODIS & AMSR2 dataset with a resolution of 1 km from the University of Bremen (Ludwig et al., 2019, 2020). During the MOSAiC period, this dataset, however, is only available until end of May 2020. Hence, from beginning of June 2020 SIC from the AMRS2 data (Spren et al., 2008) with a resolution of 3.125 km was used. The lead fraction was taken from the satellite synthetic-aperture radar derived sea ice divergence based on Sentinel-1 data (von Albedyll, 2024) as described in von Albedyll et al. (2024). Lead fraction data



225 covers the period between October 2019 and May 2020, with a gap between 14 January and 15 March 2020 when Polarstern was north of the maximum latitude of Sentinel-1. The melt-pond fraction was obtained from the Ocean and Land Colour Instrument (OLCI) data on board the Sentinel-3 satellite as described in Istomina et al. (2025).

4 Results

An overview of the MOSAiC period is shown in Fig. 2. Depicted are different parameters relevant for this study. Panel (c) summarizes the sea ice fraction (dark blue line) and the lead fraction (green dots) both within a radius of 50 km around Polarstern, together with the melt-pond fraction in an area of 100 km around Polarstern (cyan crosses). The radius for the melt-pond fraction calculation in the vicinity of Polarstern was doubled compared to the sea ice and lead fraction because the melt-pond data coverage is reduced in summer. The ice edge is defined as SIC below 50%. Rapid variability in the distance to the ice edge shown in panel (d) can be caused, for instance, by the opening of large leads or polynyas, as for example on 16 March 2020.

Three distinct warm-air intrusions (WAI) can be identified in the temperature overview (blue line in Fig. 2 (a)). The first WAI reached Polarstern during mid-end of November 2019, with temperatures at the surface above -10°C . The second WAI occurred mid-end of February 2020 with surface temperatures slightly below -10°C , and the last one during mid-end of April 2020 with temperatures close to 0°C (Dada et al., 2022; Kirbus et al., 2023). Dada et al. (2022) showed that this WAI had a significant impact on the aerosol size distribution and chemical composition. The WAI introduced a change of the atmospheric aerosol conditions in the Arctic from a Arctic haze dominated state into a more polluted state. Kirbus et al. (2023) highlighted that the warm air during this WAI was advected via two different pathways. A first intrusion starting on 15 April originated in northwestern Russia and passed the Barents Sea, while the second intrusion starting on 18 April was advected via west of Svalbard. Filter samples collected subsequent to each WAI showed elevated INP concentrations, compared to filter samples collected before the WAI (red bars in Fig. 2 (c)) and they correlate with short trajectory travel times to the ice edge (pink dots in Fig. 2 (d)).

From November 2019 until March 2020 the surface INP concentration in Fig. 2 panel (d) showed only a moderate increase from around $5 \cdot 10^{-4} \text{ L}^{-1}$ to around $1 \cdot 10^{-2} \text{ L}^{-1}$. Between March 2020 and end of May 2020 the INP concentration was rather constant, with one exception of increased values following directly the WAI mid-end of April 2020 with values of up to $1 \cdot 10^{-1} \text{ L}^{-1}$. From June on the INP concentration increased strongly from $1 \cdot 10^{-2} \text{ L}^{-1}$ to up to 10 L^{-1} in July 2020 followed by a slow decrease again.

The SIC remained close to 100% with only minor variations until mid April 2020. In late April 2020 the SIC went occasionally down to less than 80%, which was, however, attributed to wet snow rather than open water (Krumpen et al., 2021). A rapid decrease of the SIC with values below 40% was observed towards end of July 2020 when the ice floe reached the ice edge. With the relocation of Polarstern to a new floe mid of August 2020, the SIC in the vicinity of Polarstern increased again to around 100%. The highest lead fraction in the vicinity of Polarstern was 10% on 16 April 2020 during the April WAI.

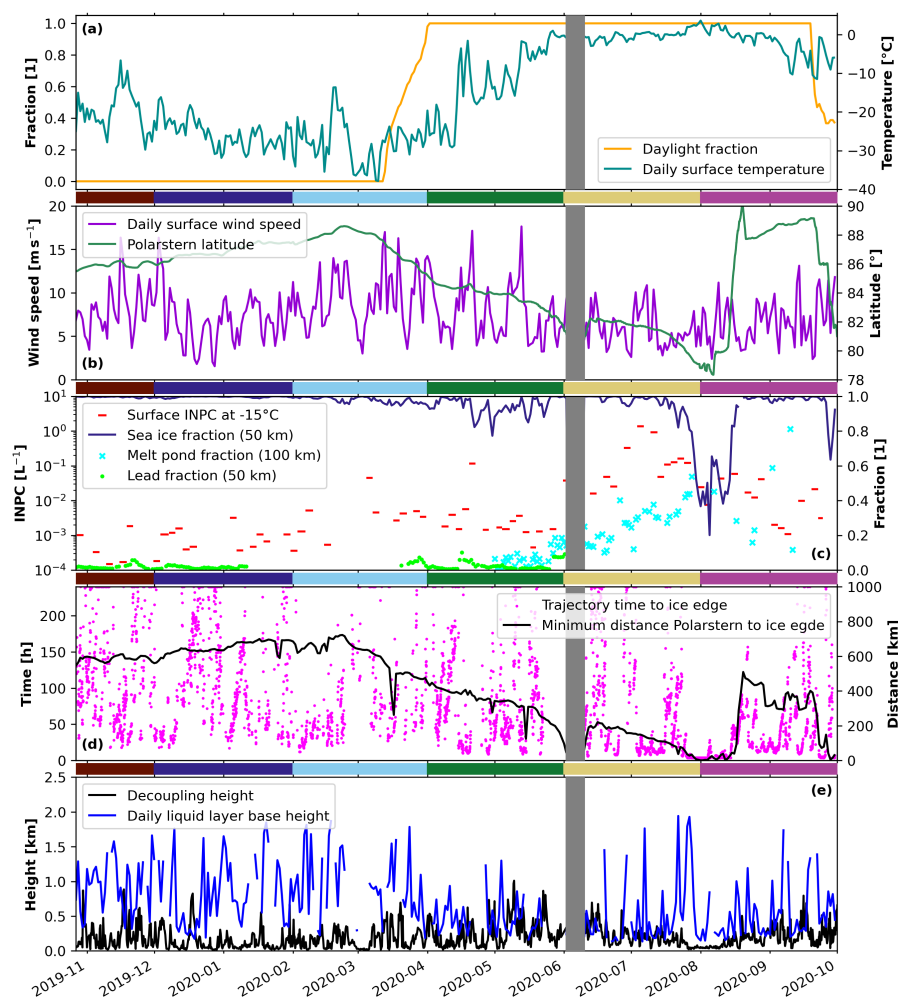


Figure 2. Overview of the MOSAiC expedition period. Panel (a) shows the theoretical daylight fraction at the position of Polarstern (orange) and the observed daily averaged surface temperature (green). In panel (b) daily averages of the surface wind (purple) and Polarstern latitude (dark green) are depicted. Panel (c) highlights the sea ice fraction (dark blue: 50 km radius), the melt pond fraction (cyan crosses: 100 km radius), and the lead fraction (green dots: 50 km radius) around Polarstern. In addition, the concentration of INPs active at -15°C measured at the surface is depicted by the red bars. In panel (d) the time in hours the backward trajectories started at the liquid layer base needed to reach the ice edge is shown by the pink dots. The black line in panel (d) shows the minimum distance of Polarstern to the ice edge. The derived decoupling height (black) and daily averaged liquid layer base height (blue) are shown in panel (e). The gray shaded period in each panel marks the period where Polarstern left the sea ice for a crew rotation between 2 June 2020 and 10 June 2020. The brown, blue, orange, green, red, and purple bars between the panels highlight the analyzed periods in Fig. 4.

However, most of the time the lead fraction was below 2%. The melt-pond fraction increased strongly from close to 0% during mid of May 2020 to more than 50% in August and September 2020.



The daily averaged liquid-dominated layer base height depicted by the blue line in Fig. 2 panel (e) is highest during winter and spring and lowest during early summer. In late summer a strong variability was observed in the base height, with mostly very low values. The derived decoupling height (black line) is lower during winter and higher during summer. However, also during winter conditions where the clouds were coupled to the SML can be identified.

4.1 Case study: ice formation at temperatures just below -5°C

Figure 3 shows a case study of a persistent low-level stratus cloud observed above Polarstern from 18 April 2020 – 18 UTC until 19 April 2020 – 15 UTC. This event was observed during the second intrusion of the April 2020 WAI, with air mass advection from the North Atlantic (Kirbus et al., 2023). Within this cloud, ice formation at temperatures slightly below -5°C was observed. The cloud phase was derived by the volume depolarization ratio below the liquid-dominated layer base (purple line in panel (a), (b), and (c)). Ice-containing clouds were identified by enhanced depolarization values, as for example most of the time from 18 April 2020 23 UTC until 19 April 2020 8 UTC. The respective cloud phase determination is highlighted at the bottom of panel (b). In panel (c) those periods that revealed a cloud radar reflectivity and hence ice occurrence which was high enough to produce a signal which should be detectable by the lidar are highlighted by the gray bars below the plot. The threshold reflectivity was derived based on the findings from Bühl et al. (2016) and the IWC-Z-T relationship presented in Hogan et al. (2006). Note, however, that the lowest detection limit of the lidar is lower than the one from the cloud radar and that the lidar may also detect ice production below the lowest detection range of the cloud radar. Hence, there can be periods where the lidar identified an ice-containing cloud but the cloud radar reflectivity was actually below the limit for lidar-based ice detection. Panel (d) shows that the derived liquid-dominated layer base was frequently below the lowest range gate of the cloud radar (e.g., on 19 April 2020 between 1 UTC and 2 UTC and later on that day between 5 UTC and 9 UTC and between 11 UTC and 15 UTC), recognizable by the height, where the Cloudnet classification mask starts.

The observed cloud was continuously below 1 km height and identified as SML-coupled cloud. Except for short periods on 19 April 2020, between 6 and 8 UTC and again between 11 and 14 UTC when some variations in the liquid-dominated layer base were observed, which caused periods where the cloud was considered as decoupled to the SML. The lidar-based cloud phase determination revealed a liquid-only cloud until 23 UTC, with a short period of ice-containing cloud around 18:30 UTC. After 23 UTC the cloud was mostly classified as ice-containing, indicated by the high volume depolarization ratio below the liquid-dominated layer base due to ice precipitation (panel (b)). The cloud minimum temperature derived as lowest temperature between liquid-dominated layer base and cloud top was continuously above -10°C , occasionally close to -5°C . The periods with derived cloud radar reflectivities that exceeded the threshold for a lidar-based ice detection correlate well with the periods where ice was detected by the lidar. However, likely due to the capabilities of the lidar to also probe lower altitudes, the lidar detected ice more frequent than periods were observed where the radar reflectivity threshold was reached.

4.2 Seasonal pattern

In Fig. 4 the fraction of ice-containing clouds as a function of their minimum temperature during the whole MOSAiC expedition for two months each is presented. The numbers above the plot indicate the cumulated hours of cloud observations, that

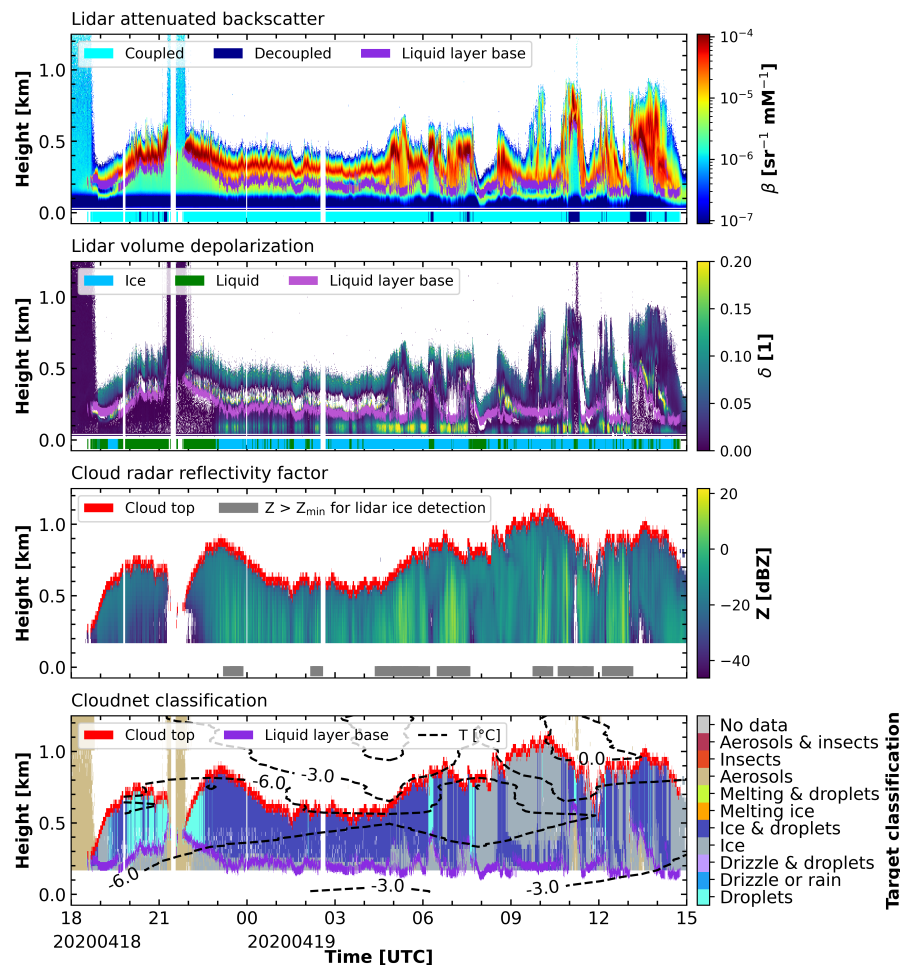


Figure 3. Ground-based remote sensing of lidar attenuated backscatter (a) and lidar volume depolarization (b), cloud radar reflectivity factor (c), and Cloudnet target classification (d) for the period of 18 April 2020 18 UTC to 19 April 2020 15 UTC. Panel (a) shows in addition the liquid-dominated layer base height (purple line) and the coupling state (light and dark blue bars at the bottom). In panel (b) additionally the liquid-dominated layer base (purple line) is shown together with the derived cloud phase depicted by the blue (ice-containing) and green (liquid) bars at the bottom. The red line in panel (c) shows the cloud top height and the gray bars at the bottom highlight periods where the cloud radar reflectivity factor met the theoretical threshold of lidar ice detection. In panel (d) the liquid-dominated layer base (purple line) and the cloud top (red line) are shown and the temperature is indicated by the dashed isotherms.

were used to derive the fraction of ice-containing clouds for the respective temperature interval during the two-month periods of the the same color code. The errors bars show the statistical uncertainty as in Seifert et al. (2010).

In October + November 2019 (brown) during 18 h of observations and in December 2019 + January 2020 (dark blue) during 295 2 h of observations, clouds with a liquid-dominated layer and a cloud minimum temperature between -15°C and -10°C were observed, but no clouds at temperatures above -10°C . In February + March 2020 (light blue) no clouds with a minimum

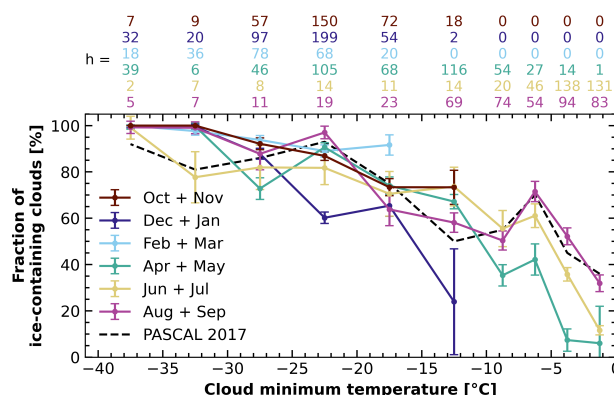


Figure 4. Fraction of ice-containing clouds observed at different cloud minimum temperature intervals during the MOSAiC year. Each colored line represents a two-month period and the black dashed line shows the fraction of ice-containing clouds observed over the Arctic ocean in summer 2017 (Griesche et al., 2021). The numbers above the plot highlight the hours of cloud observation used in the respective temperature interval in each two-month period.

temperature above -15°C were observed. In April + May 2020 (green), enhanced fraction of ice-containing clouds with a minimum temperature above -15°C was observed, with a peak between -7.5 and -5°C of 40% of ice-containing clouds. This peak corresponds to 27 h of observation. The respective signal increased through June + July 2020 (yellow, 60%, 46 h of observation) until August + September 2020 (pink) with a distinct peak of ice-containing clouds of about 70% between -7.5°C and -5°C cloud minimum temperature from 54 h of observations. For each two-month period between April and September, this peak is followed by a minimum between -10°C and -7.5°C and then a steady increase with decreasing temperature close to 100% of ice-containing clouds. These findings follow the results from Griesche et al. (2021), as indicated by the dashed black line in Fig. 4.

For a more in-depth analysis of the observed phenomena, the clouds were separated by their SML-coupling state. Figure 5 shows the same as Fig. 4 but for the months April + May (dark and light green), June + July (dark and light yellow), and August + September (dark and light purple) separated into coupled (solid lines) and decoupled (dashed lines) situations. The coupling analysis shows that the increased fraction of ice-containing clouds in April + May and June + July at low-supercooling temperatures can mostly be attributed to clouds coupled to the SML. For a cloud minimum temperature between -7.5°C and -5°C in April + May coupled clouds were observed during 22 h and 45% of the time these clouds were identified as ice-containing. Only during 5 h of observation decoupled clouds were identified, with 20% ice-containing. For June + July, decoupled clouds were found to contain ice up to 25% of the time, whereas 70% of the coupled clouds revealed to be ice-containing. In June + July decoupled clouds were observed during 11 h and coupled clouds during 35 h. In August + September, the relative difference in terms of ice fraction but also in hours of observation between coupled and decoupled clouds decreases, due to an increased fraction of ice-containing clouds in decoupled situations, compared to the months before. Under SML-

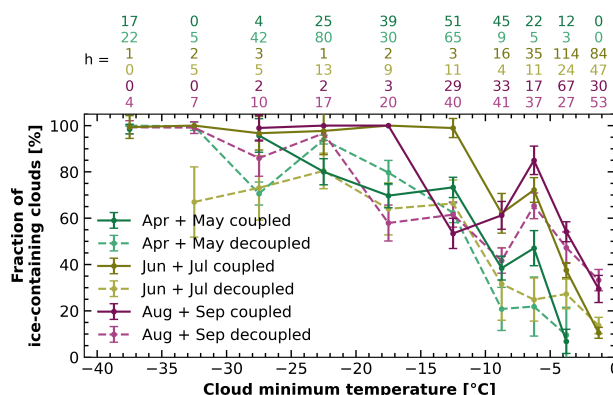


Figure 5. Same as Fig. 4 but only for April + May (light and dark green), June + July (light and dark yellow) and August + September (light and dark purple). The observations of each two-month period are separated by their coupling state, with the continuous line showing the coupled cases and the dashed lines the decoupled ones.

coupled conditions, ice was found in 85% of the clouds observed in August + September, which relates to 17 h of observation. Decoupled situations were observed during 37 h and in 65% of the time ice-containing clouds were identified.

Figure 6 shows an analysis of the free-tropospheric clouds during MOSAiC, as presented in Jimenez et al. (2025) but separated for winter (October 2019 – March 2020) and summer (April 2020 – September 2020). In the summer months, free-tropospheric ice-containing clouds were only observed with a liquid-dominated layer base above 1000 m and below -10°C . The free-tropospheric liquid-only clouds, which were observed during winter at temperatures above -10°C , were observed beginning of October 2019. At this time, the cloud radar data were not reliable (Griesche et al., 2024b). Hence, this period was not considered in the statistics presented in Fig. 4.

The free-tropospheric cloud statistics indicates that the decoupled, ice-containing clouds at $T > -10^{\circ}\text{C}$, e.g., in August + September, are mostly likely still influenced by surface processes and a clear separation from the surface is only reached in higher altitudes. This is corroborated by the histograms of liquid-dominated base height (panel (a) – (c)) and cloud minimum temperature (panel (d) – (f)) shown in Fig. 7 for coupled (dark colors) and decoupled (bright colors) clouds between April and September. In August + September the decoupled clouds showed a much lower liquid-dominated layer base height, compared to June + July, with a clear maximum below 500 m. The layer base height distribution for decoupled clouds in April + May is similar to the one for August + September. However, there is a strong difference in the cloud minimum temperature, with much colder temperatures in April + May, mostly below -10°C , while the clouds in August + September were usually observed at $T > -10^{\circ}\text{C}$.

The coupling analysis only considers the state of the cloud at the time of observation. However, clouds which were identified as decoupled above Polarstern may have been coupled to the surface before. Also a weak exchange with the SML, not covered by the applied coupling approach, can introduce alternations of the cloud properties. Therefore, a modified coupling approach was tested, to identify weakly coupled situations. The weakly coupled category was derived following Silber and

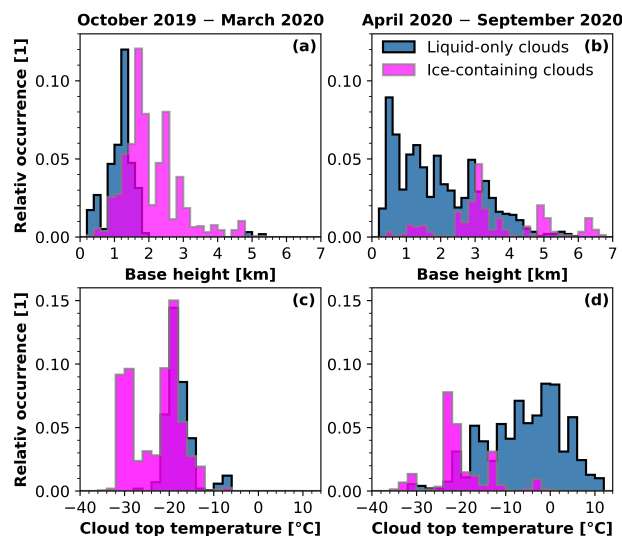


Figure 6. Histograms of liquid-dominated layer base height ((a) + (b)) and cloud top temperature ((c) + (d)) for free-tropospheric, and thus decoupled, clouds as in Jimenez et al. (2025) but separated for winter (October 2019 – March 2020, panel (a) + (c)) and summer (April 2020 – September 2020, panel (b) + (d)). Liquid-only clouds are in blue, and ice-containing clouds in pink.

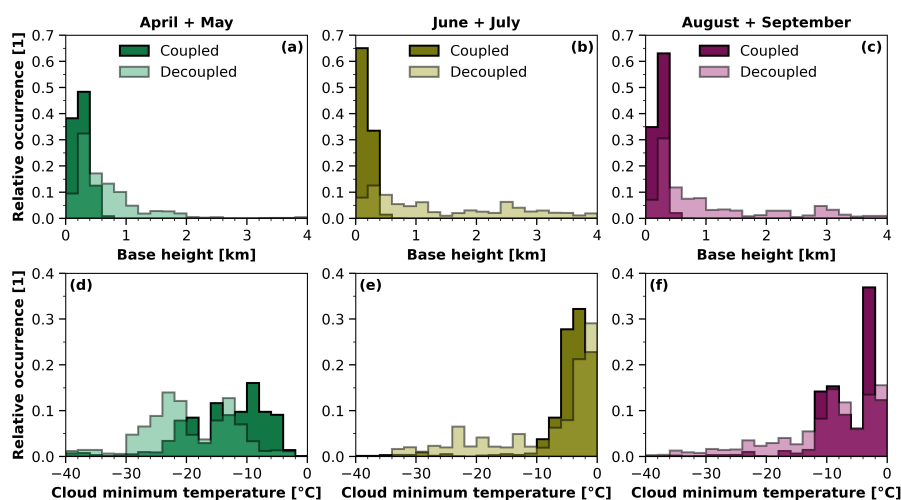


Figure 7. Histograms of liquid-dominated layer base height ((a) – (c)) and cloud minimum temperature ((d) – (f)) for April–May ((a) + (d)), June + July ((b) + (e)), and August–September ((c) + (f)). Each histogram shows the distribution for coupled (darker colors) and decoupled (brighter colors) cases.

Shupe (2022), using the ratio of the liquid-dominated layer height and the decoupling height. If this ratio was between 1 and 2, i.e., only clouds which were considered as decoupled using the approach from Sect. 3.2 were considered, a weakly coupled

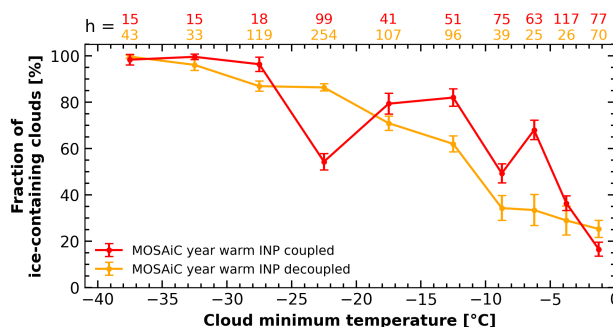


Figure 8. Same as Fig. 5 but only for days with INP active at $T > -15^{\circ}\text{C}$ detected on the filter. These days were separated by their coupling state. The red line shows data for surface coupled clouds and the yellow line for decoupled clouds.

case was defined. The results for April to September are shown in Fig. A1. The fraction of ice-containing clouds which were classified as weakly coupled (solid lines) reveals an enhanced fraction of ice-containing clouds compared to strongly decoupled clouds (dashed lines). Especially clouds observed during August + September and with a cloud minimum temperature above -7.5°C in strongly decoupled situations were noticeably reduced compared to decoupled cases in Fig. 5. In April + May and June + July, however, the frequency of ice clouds in weakly coupled situations is still much lower, compared to the coupled cases in Fig. 5.

4.3 Impact of surface INP concentrations and trajectory travel times

The surface INP measurements were used to identify days with INPs present, which activate ice formation at temperatures above -15°C and days without such warm INPs. The respective days were then analyzed for their fraction of ice-containing clouds, as done in Sect. 4.2. Clouds which were sampled during days with INPs active at $T > -15^{\circ}\text{C}$ show an increased fraction of ice-containing clouds in the temperature interval between -7.5°C and -5°C , the same interval as in Fig. 4 and Fig. 5 (not shown). During days without INPs active at $T > -15^{\circ}\text{C}$ no clouds were observed by the remote-sensing instruments (not shown). Those clouds, which were observed during days with warm INPs, were additionally separated by their coupling state. The respective fraction of ice-containing clouds is shown in Fig. 8. Unfortunately, a combined temporal and coupling state (as in Fig. 5) and INP-based separation of the dataset to analyzed the annual cycle of surface INP concentrations under coupled- and decoupled-situations on the cloud microphysics was not possible. The data coverage would have been too sparse and the resulting uncertainty would dominate any finding.

A clear separation of SML-coupled vs -decoupled clouds on days with warm INPs present at the surface is obvious in Fig. 8. SML-coupled clouds revealed a higher fraction of ice-containing clouds throughout the whole temperature range between -20°C and -5°C cloud minimum temperature, on average 17% higher. The largest difference was found for clouds with a minimum temperature between -7.5°C and -5°C with 70% of the coupled clouds were ice-containing, while only 35% of the decoupled clouds.

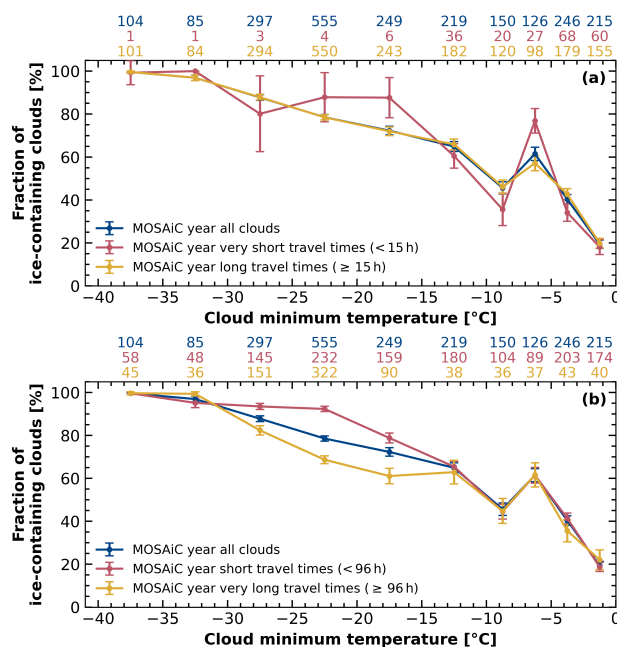


Figure 9. The blue line in panel (a) and (b) shows the fraction of ice-containing clouds for the whole MOSAiC period as a function of cloud minimum temperature. Panel (a) shows the respective analysis separated for travel times shorter (red) or longer (yellow) than 15 h, and panel (b) show the data separated for travel times shorter (red) or longer (yellow) than 96 h. The numbers above the plot highlight the hours of cloud observation used in the respective temperature interval.

Figure 9 shows the fraction of ice-containing clouds as a function of their cloud minimum temperature during the whole MOSAiC period, represented by the blue line in both panels. In each panel, additionally, the dataset separated by different respective trajectory travel times is presented. In Fig. 9 (a) the dataset was split for travel times below (red line) and above (yellow line) 15 h. This threshold was derived by a sensitivity study and was set to the time where the largest effect was found. Clouds corresponding to back-trajectories with shorter travel times to the ice edge (less or equal to 15 hours) revealed an enhanced fraction of ice-containing clouds of 80% between -7.5°C and -5°C cloud minimum temperature during 27 h of observations. This finding indicates a source of INPs close to the ice edge, e.g., in the marginal ice zone. The fraction of ice-containing clouds for travel times longer than 15 h is hardly changed compared to the whole dataset, because the fraction of clouds with travel times shorter than 15 h is rather small relative to the whole year of observation.

Travel times of more than 3 – 4 days lead to a reduction of ice-containing clouds at temperatures below -15°C , as shown in Fig 9 (b), which contrasts the observations of clouds corresponding to times below (red) and above (yellow) 96 h. Travel times shorter than 96 h increased the fraction of ice-containing clouds below -15°C . This is likely due to a depletion of long-range transported INPs, for example, via the sedimentation of a formed ice crystal. The distribution of ice-containing clouds above -15°C , however, does not change for travel times below and above 96 h, which indicates a possible resupply of INPs from the surface.



Table 3. Mean $\log_{10}(\text{EDR})$ of the uppermost 500 m (or subsection thereof in case of shallower clouds) of the clouds with cloud minimum temperature between -7.5°C and -5°C for each two-months period analyzed in Fig.5, separated by their coupling state and phase.

Cloud phase	Coupling state	April + May	June + July	August + September
Ice-containing	Coupled	−4.3	−4.43	−4.39
	Decoupled	−4.79	−4.83	−6.54
Liquid-only	Coupled	−4.7	−4.2	−5.22
	Decoupled	−5.32	−4.57	−5.75

5 Discussion

The presented analysis reveals a strong influence of the SML-coupling on the probability of clouds observed between April and September with a minimum temperature above -15°C to contain ice. From the numbers annotated above Fig. 4 it is clear that few cloud observations with cloud minimum temperature below -15°C contributed to the statistics for June + July and August + September. This is due to the fact that only the lowest liquid-containing cloud layer was analyzed. In case of multiple liquid-containing cloud layers the upper cloud was not included, as the lidar was already attenuated by the lower layer, preventing a classification of the liquid phase in the higher cloud layers. Also, no pure ice clouds were considered, as only clouds with a liquid-dominated layer were incorporated in the analysis. Another limiting factor were the relatively warm surface temperatures in July and August, often above 0°C (see Fig. 2 (a)), that caused many liquid-precipitating clouds. These clouds were removed from the analysis, as they would likely be miss-identified as pure liquid clouds by the analysis. Blowing snow was considered by removing periods with increased surface wind speed of higher than 15 m s^{-1} . Finally, all clouds that indicated potential seeder-feeder situations as described for example by Ohneiser et al. (2025b), i.e., all clouds with a second cloud within 1 km above, were also removed from the dataset.

Eddy dissipation rates (EDR) were derived from the cloud radar Doppler velocity, following Griesche et al. (2020), to investigate the influence of turbulence and thus SIP on ice occurrence. Following Chellini and Kneifel (2024), for each time step EDR in log-scale from the uppermost 500 m of the cloud were averaged. In case of a cloud top height below 500 m or a shallower cloud, the EDR of the whole cloud column until cloud top was analyzed. However, the threshold used here to separate between high and low EDR cases differed slightly, since the EDR values of the clouds analyzed in this manuscript were mostly below $10^{-3}\text{ m}^2\text{ s}^{-3}$ (upper threshold in Chellini and Kneifel (2024)). We used the 90th ($\log_{10}(\text{EDR}) > -3.47$) and the 50th ($\log_{10}(\text{EDR}) < -4.28$) percentile of all mean EDR, to separate the EDR states. Yet, no influence of the EDR on the fraction of ice-containing clouds for coupled vs decoupled clouds have been found (see Fig. A3).

The mean EDR values for coupled and decoupled clouds with temperatures between -7.5°C and -5°C in April + May, June + July, and August + September contrasted for the different cloud phases are presented in Table. 3. In general, the values are higher in case of a coupled cloud. However, in terms of cloud phase no clear picture was found. The highest EDR

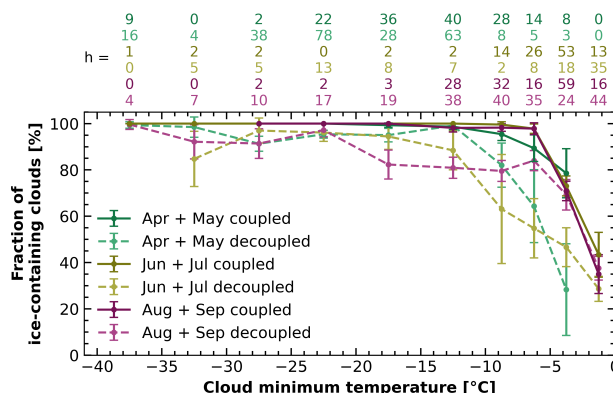


Figure 10. Same as Fig. 5 but using the cloud radar for phase separation.

values were found in coupled liquid-only clouds in June + July ($\log_{10}(\text{EDR}) = -4.2$). The lowest EDR values were found for decoupled ice-containing clouds in August + September ($\log_{10}(\text{EDR}) = -6.54$).

The applied lidar is less sensitive to ice detection as, for example, a cloud radar. The lidar was utilized due to its lower detection limit and the focus of this study, which are low-level clouds. However, the same analysis as presented in Sect. 4.2 was done using the cloud radar. The Cloudnet target classification data was used to identify ice-containing clouds. The results for all observed clouds in each two-month periods for the whole MOSAiC year is shown in Fig. A2. The results of the coupling-separated periods between April and September are shown in Fig. 10. The higher sensitivity of the cloud radar to identify ice is striking. More ice-containing clouds were identified throughout all temperature intervals and under all coupling situations. However, the coupling analysis reveals the same pattern of more ice-containing clouds under surface coupled conditions, especially at temperatures above -10°C , in all two-months periods.

The observed results of a higher fraction of ice-containing clouds under SML-coupled situations at temperatures above -15°C from April until September is a strong indicator for the impact of locally produced INPs on the cloud properties. INPs that initiate ice formation at such warm temperatures usually contain biogenic material (Pereira Freitas et al., 2023; Hartmann et al., 2025), which may come from the marginal ice zone, melt ponds, or polynyas (Irish et al., 2017; Wilson et al., 2015; Hartmann et al., 2020, 2021; Mavis et al., 2025). Creamean et al. (2022) and Barry et al. (2025) reported a maximum of INPs active above -15°C observed during MOSAiC between May and September at the surface. Under coupled situations these INPs likely got mixed into the low-level clouds and hence increased the ice occurrence in these clouds. This is supported by the strong influence of the coupling analysis on the fraction of ice-containing clouds on days where INPs active above -15°C were sampled on the ground (and thus within the boundary layer). Additionally, a back-trajectory travel time analysis revealed a decreased fraction of ice-containing clouds a temperatures below -15°C after 3 – 4 days, while no such effect was observed for clouds at higher temperatures. This can be caused, for example, by a depletion of INPs below -15°C with time and a possible resupply of INPs active above -15°C from local sources.



In August + September, however, the decoupled clouds also showed a high fraction of ice-containing clouds. The weak stability in fall during MOSAiC (Jozef et al., 2024) can support a mixing of locally produced INPs with biogenic material into the free troposphere, which would increase the availability of INPs active above -15°C . Contrasting the results of the boundary layer clouds presented in this manuscript with the free-tropospheric ones analyzed in Jimenez et al. (2025), it was shown that the decoupled clouds in August + September were often observed at rather low altitudes, which increased the likelihood of a surface influence on these clouds (see Fig. 7). Yet, increased long-range transport can also fill the respective INP reservoir in the free-troposphere. Even though Polarstern was located far in the north and even crossed the North Pole during August + September the probed air masses had rather short travel times to the measurement site (see Fig. 2).

6 Conclusions

In this study, the first annual cycle of heterogeneous ice-formation temperatures for Arctic mixed-phase clouds is presented for clouds observed during the MOSAiC year from 2019 to 2020, with a special focus on low-level clouds. It was shown that no cloud with minimum temperatures above -10°C was observed from October to end of March. From April to September, a maximum of ice-containing clouds was found between -7.5°C and -5°C . This finding indicates an influence of biogenic material containing INPs, which are needed for ice formation at these temperatures. The presented results corroborate the findings from Creamean et al. (2025) and Barry et al. (2025) who observed a peak in the INP number concentration during MOSAiC during summer.

The most relevant processes identified in this study for low-level clouds to form ice at temperatures above -10°C are summarized in Fig. 11. From October to March no clouds were observed above -10°C . However, this may change due to the changing Arctic, where the warming is most prominent in winter. From April to September, we found an increasing ice-formation efficiency at $T > -10^{\circ}\text{C}$ if the clouds were decoupled from the surface. Under conditions when clouds were coupled to the surface mixed-layer (SML), already in April efficient ice formation at $T > -10^{\circ}\text{C}$ was observed. The increased ice formation under SML-coupled situations was attributed to an increased availability of INPs that contained biogenic material in the SML, likely from local Arctic marine sources, such as the marginal ice zone. Barry et al. (2025) proved by means of heat treatments, that the INPs measured during the MOSAiC summer at the surface were almost entirely biological ones. The INPs can be mixed into the cloud if the cloud mixed layer (CML), which is driven by convection from radiative cloud top cooling, reaches the SML. The coupling of the CML to the SML was derived using the potential temperature profile from radiosonde measurements. Yet, additional relevant factors are also long-range transport and cloud top entrainment of INPs.

From April to September, the dataset was separated by the cloud SML coupling state. A strong influence on the likelihood of clouds to contain ice at high ice-formation temperatures was found from April to July. Coupled clouds showed a 2 – 3 higher probability to contain ice at $T > -15^{\circ}\text{C}$ when the cloud was coupled to the SML in these months. In August + September, the ratio of the fraction of coupled to decoupled ice-containing clouds decreased to 1.3. Similarly, from April to July, clouds were more frequently observed as coupled at $T > -15^{\circ}\text{C}$, while in August + September, the clouds were more often identified as decoupled. It is likely that the decoupled clouds in August + September are still to a significant part influenced by surface

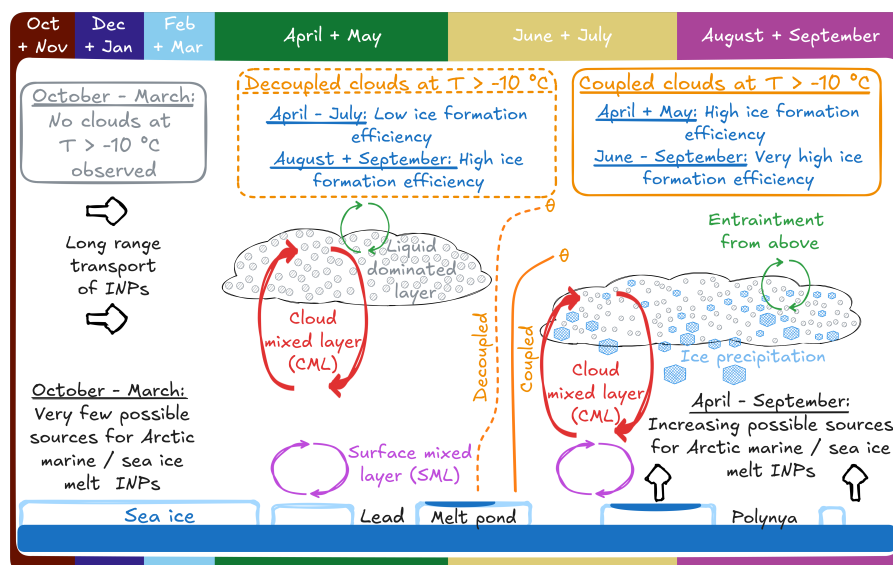


Figure 11. Idealized summary of the observed mechanisms driving heterogeneous ice formation in Arctic low-level mixed-phase clouds at $T > -10^{\circ}\text{C}$ during the MOSAiC expedition. The curved arrows indicate different relevant mixing mechanisms: entrainment from above (green), cloud mixing (red) and surface mixing (pink). Black arrows show potential pathways of INP supply in the boundary layer and free troposphere (long-range transport and local marine and sea ice melt emissions). Between October 2019 and March 2020 no clouds were observed at $T > -10^{\circ}\text{C}$. Due to a sea-ice fraction of close to 100%, absent melt ponds, and a very low lead fraction from late autumn to early spring, very few local sources of INPs can be expected during this time. From April to September, the fraction of possible sources for marine and sea ice melt INPs increased due to an increase in the lead and melt pond fraction and a decrease in sea-ice fraction with time. From April to July strong differences between coupled (solid, orange Θ profile) and decoupled (dashed, orange Θ profile) situations were found. In decoupled clouds, low ice-formation efficiency was observed for clouds at $T > -10^{\circ}\text{C}$. In coupled clouds, the ice-formation efficiency was 2 – 3 times higher between April and July. In August and September, besides coupled clouds, also decoupled clouds showed an enhanced ice formation at $T > -10^{\circ}\text{C}$.

455 processes. Weaker stability during fall may result in an increased exchange between the PBL and the free troposphere and hence a stronger transport of INPs from the surface to the free troposphere. The derived liquid-dominated layer heights were lower in August + September (mostly below 500 m) compared to June + July, resulting in more detected decoupled clouds in August + September. Additionally, the minimum temperature for the decoupled clouds in August + September was rather high (mostly above -10°C) and hence ice-formation at relatively warm subzero temperatures was likely to be observed. Yet, an
 460 increased long-range transport of INP-carrying air masses could also be the cause of the observed phenomenon. For example, Ansmann et al. (2023) showed that the free tropospheric INP load at 2000 m during the MOSAiC expedition was dominated by continental particles throughout the year.

Heterogeneous ice-formation temperatures were linked to the presence of INPs measured at the surface, using filter samples collected during MOSAiC and the coupling analysis. During days with INPs active above -15°C present at the surface, the



465 probability of clouds to contain ice at temperatures above -20°C increased. Between -7.5°C and -5°C , for example, the
 fraction of ice-containing SML-coupled clouds during days with such INPs active above -15°C was 70%, while it was 35%
 for decoupled clouds. Finally, travel times of trajectories initiated at the liquid-dominated layer base height were used to show
 that shorter travel times ($< 15\text{ h}$) correspond to an increase in the fraction of ice-containing clouds for $-7.5^{\circ}\text{C} > T > -5^{\circ}\text{C}$.
 Travel times of more than 96 h correspond to a decrease in the fraction of ice-containing clouds below -15°C , while no
 470 difference between longer or shorter travel times of 96 h was observed for clouds with $T > -15^{\circ}\text{C}$. These findings support
 the hypothesis that locally produced INPs are a major driver of the enhanced ice occurrence at low-supercooling temperatures,
 while long-range transported INPs are dominating the ice-production below -15°C .

The presented feature of increased ice formation at relatively warm subzero temperatures under SML-coupled situations
 in Arctic low-level mixed-phase clouds should be further analyzed, with a focus on contrasting Arctic and Antarctic cloud
 475 properties, given the recent changes also happening in Antarctica. Also, the development of the seasonal cycle should be
 investigated further. Under the changing conditions in the Arctic, clouds at warm subzero temperatures might be observed
 soon also in Arctic winter (Jenkins et al., 2024). Additionally, the availability of sources may change under a warming Arctic.
 Even though a clear connection between surface-based measurements of INP concentrations and cloud ice-microphysics was
 established here, not all mechanisms at play could be quantified, yet. Modeling results as well as observational datasets from
 480 campaigns but also long-term records from land-based stations should be harvested to investigate this phenomenon in more
 detail. Finally, if sources at the surface play a significant role in the cloud microphysical properties, this should reflect on
 the radiative properties of the cloud. Hence, it is worth investigating whether clouds coupled to the SML have an identifiable
 different cloud radiative effect. In this regard, the new satellite mission EarthCARE (Wehr et al., 2023) provides valuable
 opportunities.

485 *Data availability.* The lidar observations and the Cloudnet target classification is published in Engelmann et al. (2025). The cloud radar data
 is published in Lindenmaier et al. (2024). The INP concentrations are available via Hill et al. (2024) and the radiosonde data via Dahlke et al.
 (2023). The SIC is published in Ludwig et al. (2019, 2020) and is available at <https://www.seaice.uni-bremen.de>, the lead fraction in von
 Albedyll (2024), and the melt pond fraction is available via Istomina et al. (2025).

Appendix A

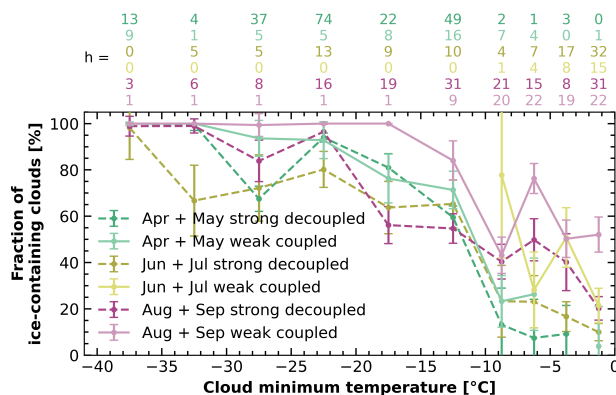


Figure A1. Same as Fig. 5 but with modified coupling approach.

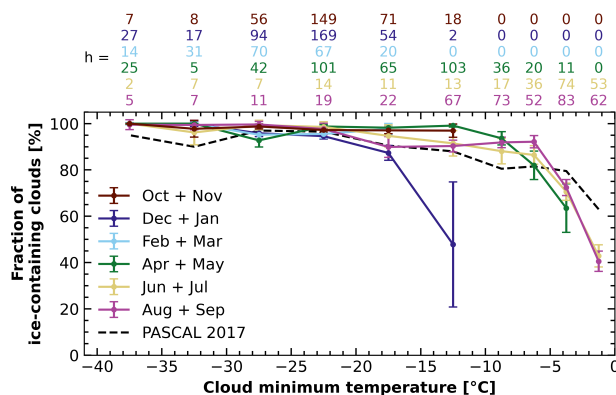


Figure A2. Same as Fig. 4 but using the cloud radar for phase separation.

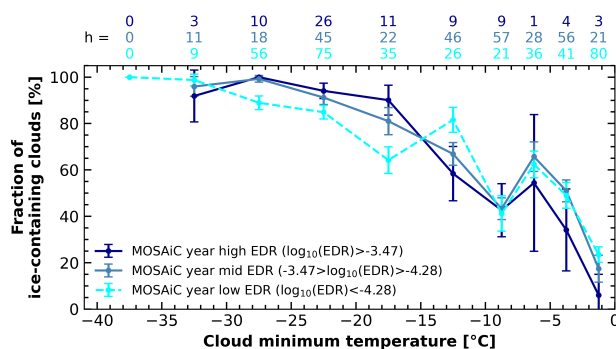


Figure A3. Fraction of ice-containing clouds as a function of their minimum temperature during the MOSAiC expedition, separated for the mean EDR observed in the upper 500 m of the cloud.



490 *Author contributions.* The paper was written and designed by HJG. The data analysis was performed by HJG, MR, AA, and PS. RE, HG, MR, JH, and DA took care of the lidar observations on board Polarstern during MOSAiC. JC, and KRB performed the INP measurements and analysis. CJ conducted the free-tropospheric clouds analysis. All coauthors were actively involved in the extended discussions and the elaboration of the final design of the article.

Competing interests. Jessie Creamean is a member of the editorial board of ACP.

495 *Acknowledgements.* Data used in this article were conducted as part of the international Multidisciplinary drifting Observatory for the Study of the Arctic Climate (MOSAiC) with the tag MOSAiC20192020 and the Project ID: AWI_PS122_00. We would like to thank everyone who contributed to the measurements used here and to the logistical support during the 1-year MOSAiC expedition (Nixdorf et al., 2021). Radiosonde data were obtained through a partnership between the leading Alfred Wegener Institute, the Atmospheric Radiation Measurement user facility, a US Department of Energy facility managed by the Biological and Environmental Research Program, and the German Weather
500 Service (DWD). We thank the U.S Department of Energy Atmospheric Systems Research program (grant nos. DE-SC0019745 and DE-SC0022046) and Atmospheric Radiation Measurement user facility (grant no DE-AC05-76RL01830). This research has been supported by the Deutsche Forschungsgemeinschaft (DFG, German Research Foundation, project no. 268020496-TRR 172) within the Transregional Collaborative Research Center “Arctic Amplification: Climate Relevant Atmospheric and SurfaCe Processes, and Feedback Mechanisms (AC)3”. Financial support was also provided by the by the European Commission project CleanCloud (grant no. 101137639).



505 References

- Akansu, E. F., Dahlke, S., Siebert, H., and Wendisch, M.: Evaluation of methods to determine the surface mixing layer height of the atmospheric boundary layer in the central Arctic during polar night and transition to polar day in cloudless and cloudy conditions, *Atmospheric Chemistry and Physics*, 23, 15 473–15 489, <https://doi.org/10.5194/acp-23-15473-2023>, 2023.
- Ansmann, A., Tesche, M., Seifert, P., Althausen, D., Engelmann, R., Fruntke, J., Wandinger, U., Mattis, I., and Müller, D.: Evolution of the ice phase in tropical altocumulus: SAMUM lidar observations over Cape Verde, *Journal of Geophysical Research: Atmospheres*, 114, <https://doi.org/10.1029/2008JD011659>, 2009.
- Ansmann, A., Ohneiser, K., Engelmann, R., Radenz, M., Griesche, H., Hofer, J., Althausen, D., Creamean, J. M., Boyer, M. C., Knopf, D. A., Dahlke, S., Maturilli, M., Gebauer, H., Bühl, J., Jimenez, C., Seifert, P., and Wandinger, U.: Annual cycle of aerosol properties over the central Arctic during MOSAiC 2019–2020 – light-extinction, CCN, and INP levels from the boundary layer to the tropopause, *Atmospheric Chemistry and Physics*, 23, 12 821–12 849, <https://doi.org/10.5194/acp-23-12821-2023>, 2023.
- Barry, K. R., Hill, T. C., Jentsch, C., Moffett, B. F., Stratmann, F., and DeMott, P. J.: Pragmatic protocols for working cleanly when measuring ice nucleating particles, *Atmospheric Research*, 250, 105 419, <https://doi.org/10.1016/j.atmosres.2020.105419>, 2021.
- Barry, K. R., Hill, T. C. J., Kreidenweis, S. M., DeMott, P. J., Tobo, Y., and Creamean, J. M.: Bioaerosols as indicators of central Arctic ice nucleating particle sources, *Atmospheric Chemistry and Physics*, 25, 11 919–11 933, <https://doi.org/10.5194/acp-25-11919-2025>, 2025.
- Bergeron, T.: On the physics of clouds and precipitation, *Proc. 5th Assembly U.G.G.I., Lisbon, Portugal*, 1935, pp. 156–180, 1935.
- Bohlmann, S., Baars, H., Radenz, M., Engelmann, R., and Macke, A.: Ship-borne aerosol profiling with lidar over the Atlantic Ocean: from pure marine conditions to complex dust–smoke mixtures, *Atmospheric Chemistry and Physics*, 18, 9661–9679, <https://doi.org/10.5194/acp-18-9661-2018>, 2018.
- Brooks, I. M., Tjernström, M., Persson, P. O. G., Shupe, M. D., Atkinson, R. A., Canut, G., Birch, C. E., Mauritsen, T., Sedlar, J., and Brooks, B. J.: The Turbulent Structure of the Arctic Summer Boundary Layer During The Arctic Summer Cloud-Ocean Study, *Journal of Geophysical Research: Atmospheres*, 122, 9685–9704, <https://doi.org/10.1002/2017JD027234>, 2017.
- Bühl, J., Seifert, P., Myagkov, A., and Ansmann, A.: Measuring ice- and liquid-water properties in mixed-phase cloud layers at the Leipzig Cloudnet station, *Atmospheric Chemistry and Physics*, 16, 10 609–10 620, <https://doi.org/10.5194/acp-16-10609-2016>, 2016.
- Chellini, G. and Kneifel, S.: Turbulence as a Key Driver of Ice Aggregation and Riming in Arctic Low-Level Mixed-Phase Clouds, Revealed by Long-Term Cloud Radar Observations, *Geophysical Research Letters*, 51, <https://doi.org/10.1029/2023gl106599>, 2024.
- Chellini, G., Gierens, R., and Kneifel, S.: Ice Aggregation in Low-Level Mixed-Phase Clouds at a High Arctic Site: Enhanced by Dendritic Growth and Absent Close to the Melting Level, *Journal of Geophysical Research: Atmospheres*, 127, e2022JD036 860, <https://doi.org/10.1029/2022JD036860>, e2022JD036860 2022JD036860, 2022.
- Creamean, J. M., Kirpes, R. M., Pratt, K. A., Spada, N. J., Maahn, M., de Boer, G., Schnell, R. C., and China, S.: Marine and terrestrial influences on ice nucleating particles during continuous springtime measurements in an Arctic oilfield location, *Atmospheric Chemistry and Physics*, 18, 18 023–18 042, <https://doi.org/10.5194/acp-18-18023-2018>, 2018.
- Creamean, J. M., Hill, T. C. J., DeMott, P. J., Uetake, J., Kreidenweis, S., and Douglas, T. A.: Thawing permafrost: an overlooked source of seeds for Arctic cloud formation, *Environmental Research Letters*, 15, 084 022, <https://doi.org/10.1088/1748-9326/ab87d3>, 2020.
- Creamean, J. M., de Boer, G., Telg, H., Mei, F., Dexheimer, D., Shupe, M. D., Solomon, A., and McComiskey, A.: Assessing the vertical structure of Arctic aerosols using balloon-borne measurements, *Atmospheric Chemistry and Physics*, 21, 1737–1757, <https://doi.org/10.5194/acp-21-1737-2021>, 2021.



- Creamean, J. M., Barry, K., Hill, T. C. J., Hume, C., DeMott, P. J., Shupe, M. D., Dahlke, S., Willmes, S., Schmale, J., Beck, I., Hoppe, C. J. M., Fong, A., Chamberlain, E., Bowman, J., Scharien, R., and Persson, O.: Annual cycle observations of aerosols capable of ice formation in central Arctic clouds, *Nature Communications*, 13, <https://doi.org/10.1038/s41467-022-31182-x>, 2022.
- 545 Creamean, J. M., Hume, C. C., Vazquez, M., and Theisen, A.: Long-term measurements of ice nucleating particles at Atmospheric Radiation Measurement (ARM) sites worldwide, *Earth Syst. Sci. Data Discuss.*, <https://doi.org/10.5194/essd-2025-352>, 2025.
- Dada, L., Angot, H., Beck, I., Baccarini, A., Quéléver, L. L. J., Boyer, M., Laurila, T., Brasseur, Z., Jozef, G., de Boer, G., Shupe, M. D., Henning, S., Bucci, S., Dütsch, M., Stohl, A., Petäjä, T., Daellenbach, K. R., Jokinen, T., and Schmale, J.: A central arctic extreme aerosol event triggered by a warm air-mass intrusion, *Nature Communications*, 13, <https://doi.org/10.1038/s41467-022-32872-2>, 2022.
- 550 Dahlke, S., Shupe, M. D., Cox, C. J., Brooks, I. M., Blomquist, B., and Persson, P. O. G.: Extended radiosonde profiles 2019/09-2020/10 during MOSAiC Legs PS122/1 - PS122/5, <https://doi.org/10.1594/PANGAEA.961881>, 2023.
- DeMott, P. J., Hill, T. C. J., McCluskey, C. S., Prather, K. A., Collins, D. B., Sullivan, R. C., Ruppel, M. J., Mason, R. H., Irish, V. E., Lee, T., Hwang, C. Y., Rhee, T. S., Snider, J. R., McMeeking, G. R., Dhaniyala, S., Lewis, E. R., Wentzell, J. J. B., Abbatt, J., Lee, C., Sultana, C. M., Ault, A. P., Axson, J. L., Diaz Martinez, M., Venero, I., Santos-Figueroa, G., Stokes, M. D., Deane, G. B., Mayol-Bracero, O. L.,
- 555 Grassian, V. H., Bertram, T. H., Bertram, A. K., Moffett, B. F., and Franc, G. D.: Sea spray aerosol as a unique source of ice nucleating particles, *Proceedings of the National Academy of Sciences*, 113, 5797–5803, <https://doi.org/10.1073/pnas.1514034112>, 2016.
- Egerer, U., Gottschalk, M., Siebert, H., Ehrlich, A., and Wendisch, M.: The new BELUGA setup for collocated turbulence and radiation measurements using a tethered balloon: first applications in the cloudy Arctic boundary layer, *Atmospheric Measurement Techniques*, 12, 4019–4038, <https://doi.org/10.5194/amt-12-4019-2019>, 2019.
- 560 Egerer, U., Ehrlich, A., Gottschalk, M., Griesche, H., Neggers, R. A. J., Siebert, H., and Wendisch, M.: Case study of a humidity layer above Arctic stratocumulus and potential turbulent coupling with the cloud top, *Atmospheric Chemistry and Physics*, 21, 6347–6364, <https://doi.org/10.5194/acp-21-6347-2021>, 2021.
- Eirund, G. K., Possner, A., and Lohmann, U.: Response of Arctic mixed-phase clouds to aerosol perturbations under different surface forcings, *Atmospheric Chemistry and Physics*, 19, 9847–9864, <https://doi.org/10.5194/acp-19-9847-2019>, 2019.
- 565 Engelmann, R., Kanitz, T., Baars, H., Heese, B., Althausen, D., Skupin, A., Wandinger, U., Komppula, M., Stachlewska, I. S., Amiridis, V., Marinou, E., Mattis, I., Linné, H., and Ansmann, A.: The automated multiwavelength Raman polarization and water-vapor lidar Polly^{XT}: the neXT generation, *Atmospheric Measurement Techniques*, 9, 1767–1784, <https://doi.org/10.5194/amt-9-1767-2016>, 2016.
- Engelmann, R., Ansmann, A., Ohneiser, K., Griesche, H., Radenz, M., Hofer, J., Althausen, D., Dahlke, S., Maturilli, M., Veselovskii, I., Jimenez, C., Wiesen, R., Baars, H., Bühl, J., Gebauer, H., Haarig, M., Seifert, P., Wandinger, U., and Macke, A.: Wildfire smoke, Arctic
- 570 haze, and aerosol effects on mixed-phase and cirrus clouds over the North Pole region during MOSAiC: an introduction, *Atmospheric Chemistry and Physics*, 21, 13 397–13 423, <https://doi.org/10.5194/acp-21-13397-2021>, 2021.
- Engelmann, R., Althausen, D., Baars, H., Griesche, H., Hofer, J., Radenz, M., and Seifert, P.: Custom collection of categorize, classification, droplet effective radius, ice effective radius, ice water content, and 2 other products from RV Polarstern between 27 Oct 2019 and 1 Oct 2020, <https://doi.org/10.60656/5B9EC816419A4027>, 2025.
- 575 Findeisen, W.: Die kolloidmeteorologischen Vorgänge bei der Niederschlagsbildung, *Meteorologische Zeitschrift*, 55, 121–133, 1938.
- Gierens, R., Kneifel, S., Shupe, M. D., Ebell, K., Maturilli, M., and Löhnert, U.: Low-level mixed-phase clouds in a complex Arctic environment, *Atmospheric Chemistry and Physics*, 20, 3459–3481, <https://doi.org/10.5194/acp-20-3459-2020>, 2020.



- Griesche, H. J., Seifert, P., Ansmann, A., Baars, H., Barrientos Velasco, C., Bühl, J., Engelmann, R., Radenz, M., Zhenping, Y., and Macke, A.: Application of the shipborne remote sensing supersite OCEANET for profiling of Arctic aerosols and clouds during *Polarstern* cruise PS106, *Atmospheric Measurement Techniques*, 13, 5335–5358, <https://doi.org/10.5194/amt-13-5335-2020>, 2020.
- Griesche, H. J., Ohneiser, K., Seifert, P., Radenz, M., Engelmann, R., and Ansmann, A.: Contrasting ice formation in Arctic clouds: surface-coupled vs. surface-decoupled clouds, *Atmospheric Chemistry and Physics*, 21, 10 357–10 374, <https://doi.org/10.5194/acp-21-10357-2021>, 2021.
- Griesche, H. J., Barrientos-Velasco, C., Deneke, H., Hünenbein, A., Seifert, P., and Macke, A.: Low-level Arctic clouds: a blind zone in our knowledge of the radiation budget, *Atmospheric Chemistry and Physics*, 24, 597–612, <https://doi.org/10.5194/acp-24-597-2024>, 2024a.
- Griesche, H. J., Seifert, P., Engelmann, R., Radenz, M., Hofer, J., Althausen, D., Walbröl, A., Barrientos-Velasco, C., Baars, H., Dahlke, S., Tukiainen, S., and Macke, A.: Cloud micro- and macrophysical properties from ground-based remote sensing during the MOSAiC drift experiment, *Scientific Data*, 11, <https://doi.org/10.1038/s41597-024-03325-w>, 2024b.
- Hartmann, M., Adachi, K., Eppers, O., Haas, C., Herber, A., Holzinger, R., Hünenbein, A., Jäkel, E., Jentsch, C., van Pinxteren, M., Wex, H., Willmes, S., and Stratmann, F.: Wintertime Airborne Measurements of Ice Nucleating Particles in the High Arctic: A Hint to a Marine, Biogenic Source for Ice Nucleating Particles, *Geophysical Research Letters*, 47, e2020GL087 770, <https://doi.org/10.1029/2020GL087770>, e2020GL087770 10.1029/2020GL087770, 2020.
- Hartmann, M., Gong, X., Kecorius, S., van Pinxteren, M., Vogl, T., Welti, A., Wex, H., Zeppenfeld, S., Herrmann, H., Wiedensohler, A., and Stratmann, F.: Terrestrial or marine – indications towards the origin of ice-nucleating particles during melt season in the European Arctic up to 83.7° N, *Atmospheric Chemistry and Physics*, 21, 11 613–11 636, <https://doi.org/10.5194/acp-21-11613-2021>, 2021.
- Hartmann, S., Schrödner, R., Hassett, B. T., Hartmann, M., van Pinxteren, M., Fomba, K. W., Stratmann, F., Herrmann, H., Pöhlker, M., and Zeppenfeld, S.: Polysaccharides-Important Constituents of Ice-Nucleating Particles of Marine Origin, *Environmental Science & Technology*, 59, 5098–5108, <https://doi.org/10.1021/acs.est.4c08014>, 2025.
- Hill, T., DeMott, P., and Creamean, J.: MOSAiC-Colorado State University Ice Spectrometer, <https://doi.org/10.5439/1804484>, 2024.
- Hogan, R. J., Mittermaier, M. P., and Illingworth, A. J.: The Retrieval of Ice Water Content from Radar Reflectivity Factor and Temperature and Its Use in Evaluating a Mesoscale Model, *Journal of Applied Meteorology and Climatology*, 45, 301–317, <https://doi.org/10.1175/JAM2340.1>, 2006.
- Hoose, C. and Möhler, O.: Heterogeneous ice nucleation on atmospheric aerosols: a review of results from laboratory experiments, *Atmospheric Chemistry and Physics*, 12, 9817–9854, <https://doi.org/10.5194/acp-12-9817-2012>, 2012.
- Igel, A. L., Ekman, A. M. L., Leck, C., Tjernström, M., Savre, J., and Sedlar, J.: The free troposphere as a potential source of arctic boundary layer aerosol particles, *Geophysical Research Letters*, 44, 7053–7060, <https://doi.org/10.1002/2017gl073808>, 2017.
- Illingworth, A. J., Hogan, R. J., O'Connor, E., Bouniol, D., Brooks, M. E., Delanoé, J., Donovan, D. P., Eastment, J. D., Gaussiat, N., Goddard, J. W. F., Haefelin, M., Baltink, H. K., Krasnov, O. A., Pelon, J., Piriou, J.-M., Protat, A., Russchenberg, H. W. J., Seifert, A., Tompkins, A. M., van Zadelhoff, G.-J., Vinit, F., Willén, U., Wilson, D. R., and Wrench, C. L.: Cloudnet, *Bulletin of the American Meteorological Society*, 88, 883–898, <https://doi.org/10.1175/BAMS-88-6-883>, 2007.
- Irish, V. E., Elizondo, P., Chen, J., Chou, C., Charette, J., Lizotte, M., Ladino, L. A., Wilson, T. W., Gosselin, M., Murray, B. J., Polishchuk, E., Abbatt, J. P. D., Miller, L. A., and Bertram, A. K.: Ice-nucleating particles in Canadian Arctic sea-surface microlayer and bulk seawater, *Atmospheric Chemistry and Physics*, 17, 10 583–10 595, <https://doi.org/10.5194/acp-17-10583-2017>, 2017.
- Istomina, L., Niehaus, H., and Spreen, G.: Updated Arctic melt pond fraction dataset and trends 2002–2023 using ENVISAT and Sentinel-3 remote sensing data, *The Cryosphere*, 19, 83–105, <https://doi.org/10.5194/tc-19-83-2025>, 2025.



- Jenkins, M. T., Dai, A., and Deser, C.: Seasonal Variations and Spatial Patterns of Arctic Cloud Changes in Association with Sea Ice Loss during 1950–2019 in ERA5, *Journal of Climate*, 37, 735 – 754, <https://doi.org/10.1175/JCLI-D-23-0117.1>, 2024.
- Jensen, M. P., Holdridge, D. J., Survo, P., Lehtinen, R., Baxter, S., Toto, T., and Johnson, K. L.: Comparison of Vaisala radiosondes RS41 and RS92 at the ARM Southern Great Plains site, *Atmospheric Measurement Techniques*, 9, 3115–3129, <https://doi.org/10.5194/amt-9-3115-2016>, 2016.
- Jimenez, C., Ansmann, A., Engelmann, R., Donovan, D., Malinka, A., Schmidt, J., Seifert, P., and Wandinger, U.: The dual-field-of-view polarization lidar technique: a new concept in monitoring aerosol effects in liquid-water clouds – theoretical framework, *Atmospheric Chemistry and Physics*, 20, 15 247–15 263, <https://doi.org/10.5194/acp-20-15247-2020>, 2020.
- Jimenez, C., Ansmann, A., Ohneiser, K., Griesche, H., Engelmann, R., Radenz, M., Hofer, J., Althausen, D., Knopf, D. A., Dahlke, S., Bühl, J., Baars, H., Seifert, P., and Wandinger, U.: MOSAiC studies of long-lasting mixed-phase cloud events and analysis of the liquid-phase properties of Arctic clouds, *Atmospheric Chemistry and Physics*, <https://doi.org/10.5194/acp-25-12955-2025>, 2025.
- Jozef, G. C., Cassano, J. J., Dahlke, S., Dice, M., Cox, C. J., and de Boer, G.: An overview of the vertical structure of the atmospheric boundary layer in the central Arctic during MOSAiC, *Atmospheric Chemistry and Physics*, 24, 1429–1450, <https://doi.org/10.5194/acp-24-1429-2024>, 2024.
- Kalesse, H., de Boer, G., Solomon, A., Oue, M., Ahlgrimm, M., Zhang, D., Shupe, M. D., Luke, E., and Protat, A.: Understanding Rapid Changes in Phase Partitioning between Cloud Liquid and Ice in Stratiform Mixed-Phase Clouds: An Arctic Case Study, *Monthly Weather Review*, 144, 4805–4826, <https://doi.org/10.1175/MWR-D-16-0155.1>, 2016.
- Kanitz, T., Ansmann, A., Engelmann, R., and Althausen, D.: North-south cross sections of the vertical aerosol distribution over the Atlantic Ocean from multiwavelength Raman/polarization lidar during Polarstern cruises, *Journal of Geophysical Research: Atmospheres*, 118, 2643–2655, <https://doi.org/10.1002/jgrd.50273>, 2013.
- Kanji, Z. A., Ladino, L. A., Wex, H., Boose, Y., Burkert-Kohn, M., Czicz, D. J., and Krämer, M.: Overview of Ice Nucleating Particles, *Meteorological Monographs*, 58, 1.1 – 1.33, <https://doi.org/10.1175/AMSMONOGRAPH-D-16-0006.1>, 2017.
- Kirbus, B., Tiedeck, S., Camplani, A., Chylik, J., Crewell, S., Dahlke, S., Ebell, K., Gorodetskaya, I., Griesche, H., Handorf, D., Höschel, I., Lauer, M., Neggers, R., Rückert, J., Shupe, M. D., Spreen, G., Walbröl, A., Wendisch, M., and Rinke, A.: Surface impacts and associated mechanisms of a moisture intrusion into the Arctic observed in mid-April 2020 during MOSAiC, *Frontiers in Earth Science*, 11, <https://doi.org/10.3389/feart.2023.1147848>, 2023.
- Kiszler, T., Ori, D., and Schemann, V.: Microphysical processes involving the vapour phase dominate in simulated low-level Arctic clouds, *Atmospheric Chemistry and Physics*, 24, 10 039–10 053, <https://doi.org/10.5194/acp-24-10039-2024>, 2024.
- Kollias, P., Clothiaux, E. E., Ackerman, T. P., Albrecht, B. A., Widener, K. B., Moran, K. P., Luke, E. P., Johnson, K. L., Bharadwaj, N., Mead, J. B., Miller, M. A., Verlinde, J., Marchand, R. T., and Mace, G. G.: Development and Applications of ARM Millimeter-Wavelength Cloud Radars, *Meteorological Monographs*, 57, 17.1 – 17.19, <https://doi.org/10.1175/AMSMONOGRAPH-D-15-0037.1>, 2016.
- Krumpen, T., von Albedyll, L., Goessling, H. F., Hendricks, S., Juhls, B., Spreen, G., Willmes, S., Belter, H. J., Dethloff, K., Haas, C., Kaleschke, L., Katlein, C., Tian-Kunze, X., Ricker, R., Rostovsky, P., Rückert, J., Singha, S., and Sokolova, J.: MOSAiC drift expedition from October 2019 to July 2020: sea ice conditions from space and comparison with previous years, *The Cryosphere*, 15, 3897–3920, <https://doi.org/10.5194/tc-15-3897-2021>, 2021.
- Lac, J., Chepfer, H., Shupe, M. D., and Griesche, H.: Understanding the Spring Cloud Onset over the Arctic sea-ice, *EGUsphere*, <https://doi.org/10.5194/egusphere-2025-3549>, 2025.



- Lindenmaier, I., Feng, Y.-C., Johnson, K., Nelson, D., Isom, B., Hardin, J., Matthews, A., Wendler, T., Castro, V., and Deng, M.: Ka ARM Zenith Radar (KAZRCFRGE), <https://doi.org/10.5439/1498936>, 2024.
- 655 Lonardi, M., Pilz, C., Akansu, E. F., Dahlke, S., Egerer, U., Ehrlich, A., Griesche, H., Heymsfield, A. J., Kirbus, B., Schmitt, C. G., Shupe, M. D., Siebert, H., Wehner, B., and Wendisch, M.: Tethered balloon-borne profile measurements of atmospheric properties in the cloudy atmospheric boundary layer over the Arctic sea ice during MOSAiC: Overview and first results, *Elementa: Science of the Anthropocene*, 10, <https://doi.org/10.1525/elementa.2021.000120>, 000120, 2022.
- Ludwig, V., Spreen, G., Haas, C., Istomina, L., Kauker, F., and Murashkin, D.: The 2018 North Greenland polynya observed by a newly introduced merged optical and passive microwave sea-ice concentration dataset, *The Cryosphere*, 13, 2051–2073, <https://doi.org/10.5194/tc-13-2051-2019>, 2019.
- 660 Ludwig, V., Spreen, G., and Pedersen, L. T.: Evaluation of a New Merged Sea-Ice Concentration Dataset at 1 km Resolution from Thermal Infrared and Passive Microwave Satellite Data in the Arctic, *Remote Sensing*, 12, 3183, <https://doi.org/10.3390/rs12193183>, 2020.
- Maherndl, N., Moser, M., Schirmacher, I., Bansemmer, A., Lucke, J., Voigt, C., and Maahn, M.: How does riming influence the observed spatial variability of ice water in mixed-phase clouds?, *Atmospheric Chemistry and Physics*, 24, 13 935–13 960, <https://doi.org/10.5194/acp-24-13935-2024>, 2024.
- 665 Mavis, C. E., Vazquez, M., Bekemeier, C. A., Barry, K. R., Chamberlain, E. J., Schmale, J., Jokinen, T., Laurila, T., Shupe, M. D., Hoppe, C. J. M., Fong, A. A., Oggier, M., Ulfso, A., Balmonte, J. P., Bowman, J., Hill, T. C. J., DeMott, P. J., Kreidenweis, S. M., and Creamean, J. M.: Meltwater as a Local Source of Ice Nucleating Particles in the Central Arctic Summer, *ESS Open Archive*, <https://doi.org/10.22541/essoar.175408160.06725900/v1>, 2025.
- 670 Morrison, H., de Boer, G., Feingold, G., Harrington, J., Shupe, M. D., and Sulia, K.: Resilience of persistent Arctic mixed-phase clouds, *Nature Geoscience*, 5, 11–17, <https://doi.org/10.1038/ngeo1332>, 2012.
- Murray, B. J., O’Sullivan, D., Atkinson, J. D., and Webb, M. E.: Ice nucleation by particles immersed in supercooled cloud droplets, *Chem. Soc. Rev.*, 41, 6519–6554, <https://doi.org/10.1039/C2CS35200A>, 2012.
- 675 Neggers, R. A. J., Chylik, J., Egerer, U., Griesche, H., Schemann, V., Seifert, P., Siebert, H., and Macke, A.: Local and Remote Controls on Arctic Mixed-Layer Evolution, *Journal of Advances in Modeling Earth Systems*, 11, 2214–2237, <https://doi.org/10.1029/2019MS001671>, 2019.
- Nixdorf, U., Dethloff, K., Rex, M., Shupe, M., Sommerfeld, A., Perovich, D. K., Nicolaus, M., Heuzé, C., Rabe, B., Loose, B., Damm, E., Gradinger, R., Fong, A., Maslowski, W., Rinke, A., Kwok, R., Spreen, G., Wendisch, M., Herber, A., Hirsekorn, M., Mohaupt, V., Frickenhaus, S., Immerz, A., Weiss-Tuider, K., König, B., Mengedoht, D., Regnery, J., Gerchow, P., Ransby, D., Krumpen, T., Morgenstern, A., Haas, C., Kanzow, T., Rack, F. R., Saitzev, V., Sokolov, V., Makarov, A., Schwarze, S., Wunderlich, T., Wurr, K., and Boetius, A.: MOSAiC Extended Acknowledgement, <https://doi.org/10.5281/ZENODO.5179738>, 2021.
- 680 Ohneiser, K., Hartmann, M., Wex, H., Seifert, P., Hardt, A., Miller, A., Baudrexl, K., Thomas, W., Ettrichrätz, V., Maahn, M., Gaudek, T., Schimmel, W., Senf, F., Griesche, H., Radenz, M., and Henneberger, J.: Ice-nucleating particle depletion in the wintertime boundary layer in the pre-Alpine region during stratus cloud conditions, *EGUsphere*, <https://doi.org/10.5194/egusphere-2025-3675>, 2025a.
- 685 Ohneiser, K., Seifert, P., Schimmel, W., Senf, F., Gaudek, T., Radenz, M., Teisseire, A., Ettrichrätz, V., Vogl, T., Maherndl, N., Pfeifer, N., Henneberger, J., Miller, A. J., Omanovic, N., Fuchs, C., Zhang, H., Ramelli, F., Spirig, R., Kötsche, A., Kalesse-Los, H., Maahn, M., Corden, H., Berne, A., Hajipour, M., Griesche, H., Hofer, J., Engelmann, R., Skupin, A., Ansmann, A., and Baars, H.: Impact of seeder-feeder cloud interaction on precipitation formation: a case study based on extensive remote-sensing, in-situ and model data, *EGUsphere*, <https://doi.org/10.5194/egusphere-2025-2482>, 2025b.
- 690



- Papakonstantinou-Presvelou, I., Sourdeval, O., and Quaas, J.: Strong Ocean/Sea-Ice Contrasts Observed in Satellite-Derived Ice Crystal Number Concentrations in Arctic Ice Boundary-Layer Clouds, *Geophysical Research Letters*, 49, e2022GL098207, <https://doi.org/10.1029/2022GL098207>, 2022.
- Pasquier, J. T., Henneberger, J., Ramelli, F., Lauber, A., David, R. O., Wieder, J., Carlsen, T., Gierens, R., Maturilli, M., and Lohmann, U.:
695 Conditions favorable for secondary ice production in Arctic mixed-phase clouds, *Atmospheric Chemistry and Physics*, 22, 15 579–15 601, <https://doi.org/10.5194/acp-22-15579-2022>, 2022.
- Pereira Freitas, G., Adachi, K., Conen, F., Heslin-Rees, D., Krejci, R., Tobo, Y., Yttri, K. E., and Zieger, P.: Regionally sourced bioaerosols drive high-temperature ice nucleating particles in the Arctic, *Nature Communications*, 14, <https://doi.org/10.1038/s41467-023-41696-7>, 2023.
- 700 Porter, G. C. E., Adams, M. P., Brooks, I. M., Ickes, L., Karlsson, L., Leck, C., Salter, M. E., Schmale, J., Siegel, K., Sikora, S. N. F., Tarn, M. D., Vüllers, J., Wernli, H., Zieger, P., Zinke, J., and Murray, B. J.: Highly Active Ice-Nucleating Particles at the Summer North Pole, *Journal of Geophysical Research: Atmospheres*, 127, <https://doi.org/10.1029/2021jd036059>, 2022.
- Radenz, M., Bühl, J., Seifert, P., Baars, H., Engelmann, R., Barja González, B., Mamouri, R.-E., Zamorano, F., and Ansmann, A.: Hemispheric contrasts in ice formation in stratiform mixed-phase clouds: disentangling the role of aerosol and dynamics with ground-based
705 remote sensing, *Atmospheric Chemistry and Physics*, 21, 17 969–17 994, <https://doi.org/10.5194/acp-21-17969-2021>, 2021.
- Radenz, M., Engelmann, R., Henning, S., Schmithüsen, H., Baars, H., Frey, M. M., Weller, R., Bühl, J., Jimenez, C., Roschke, J., Muser, L. O., Wullenweber, N., Zeppenfeld, S., Griesche, H., Wandinger, U., and Seifert, P.: Ground-Based Remote Sensing of Aerosol, Clouds, Dynamics, and Precipitation in Antarctica: First Results from the 1-Year COALA Campaign at Neumayer Station III in 2023, *Bulletin of the American Meteorological Society*, 105, E1438–E1457, <https://doi.org/10.1175/bams-d-22-0285.1>, 2024.
- 710 Saavedra Garfias, P., Kalesse-Los, H., von Albedyll, L., Griesche, H., and Spreen, G.: Asymmetries in cloud microphysical properties ascribed to sea ice leads via water vapour transport in the central Arctic, *Atmospheric Chemistry and Physics*, 23, 14 521–14 546, <https://doi.org/10.5194/acp-23-14521-2023>, 2023.
- Schmale, J., Zieger, P., and Ekman, A. M. L.: Aerosols in current and future Arctic climate, *Nature Climate Change*, 11, 95–105, <https://doi.org/10.1038/s41558-020-00969-5>, 2021.
- 715 Sedlar, J., Shupe, M. D., and Tjernström, M.: On the Relationship between Thermodynamic Structure and Cloud Top, and Its Climate Significance in the Arctic, *Journal of Climate*, 25, 2374–2393, <https://doi.org/10.1175/jcli-d-11-00186.1>, 2012.
- Seidel, C., Althausen, D., Ansmann, A., Wendisch, M., Griesche, H., Radenz, M., Hofer, J., Dahlke, S., Maturilli, M., Walbröl, A., Baars, H., and Engelmann, R.: Close Correlation Between Vertically Integrated Tropospheric Water Vapor and the Downward, Broadband Thermal-Infrared Irradiance at the Ground: Observations in the Central Arctic During MOSAiC, *Journal of Geophysical Research: Atmospheres*,
720 130, <https://doi.org/10.1029/2024jd042378>, 2025.
- Seifert, P., Ansmann, A., Mattis, I., Wandinger, U., Tesche, M., Engelmann, R., Müller, D., Pérez, C., and Haustein, K.: Saharan dust and heterogeneous ice formation: Eleven years of cloud observations at a central European EARLINET site, *J. Geophys. Res.*, 115, D20 201, <https://doi.org/10.1029/2009jd013222>, 2010.
- Shaw, J., McGraw, Z., Bruno, O., Storelvmo, T., and Hofer, S.: Using Satellite Observations to Evaluate Model Microphysical Representation
725 of Arctic Mixed-Phase Clouds, *Geophysical Research Letters*, 49, <https://doi.org/10.1029/2021gl096191>, 2022.
- Shupe, M. D., Kollias, P., Matrosov, S. Y., and Schneider, T. L.: Deriving Mixed-Phase Cloud Properties from Doppler Radar Spectra, *Journal of Atmospheric and Oceanic Technology*, 21, 660–670, [https://doi.org/10.1175/1520-0426\(2004\)021<0660:DMCPFD>2.0.CO;2](https://doi.org/10.1175/1520-0426(2004)021<0660:DMCPFD>2.0.CO;2), 2004.



- Shupe, M. D., Kollias, P., Poellot, M., and Eloranta, E.: On Deriving Vertical Air Motions from Cloud Radar Doppler Spectra, *Journal of Atmospheric and Oceanic Technology*, 25, 547–557, <https://doi.org/10.1175/2007jtecha1007.1>, 2008.
- 730 Shupe, M. D., Persson, P. O. G., Brooks, I. M., Tjernstrom, M., Sedlar, J., Mauritsen, T., Sjogren, S., and Leck, C.: Cloud and boundary layer interactions over the Arctic sea ice in late summer, *Atmospheric Chemistry and Physics*, 13, 9379–9399, <https://doi.org/10.5194/acp-13-9379-2013>, 2013.
- Shupe, M. D., Rex, M., Blomquist, B., Persson, P. O. G., Schmale, J., Uttal, T., Althausen, D., Angot, H., Archer, S., Bariteau, L., Beck, I., Bilberry, J., Bucci, S., Buck, C., Boyer, M., Brasseur, Z., Brooks, I. M., Calmer, R., Cassano, J., Castro, V., Chu, D., Costa, D., Cox, C. J., Creamean, J., Crewell, S., Dahlke, S., Damm, E., de Boer, G., Deckelmann, H., Dethloff, K., Dütsch, M., Ebell, K., Ehrlich, A., Ellis, J., Engelmann, R., Fong, A. A., Frey, M. M., Gallagher, M. R., Ganzeveld, L., Gradinger, R., Graeser, J., Greenamyre, V., Griesche, H., Griffiths, S., Hamilton, J., Heinemann, G., Helmig, D., Herber, A., Heuzé, C., Hofer, J., Houchens, T., Howard, D., Inoue, J., Jacobi, H.-W., Jaiser, R., Jokinen, T., Jourdan, O., Jozef, G., King, W., Kirchgaessner, A., Klingebiel, M., Krassovski, M., Krumpfen, T., Lampert, A., Landing, W., Laurila, T., Lawrence, D., Lonardi, M., Loose, B., Lüpkes, C., Maahn, M., Macke, A., Maslowski, W., Marsay, C., Maturilli, M., Mech, M., Morris, S., Moser, M., Nicolaus, M., Ortega, P., Osborn, J., Pätzold, F., Perovich, D. K., Petäjä, T., Pilz, C., Pirazzini, R., Posman, K., Powers, H., Pratt, K. A., Preußner, A., Quéléver, L., Radenz, M., Rabe, B., Rinke, A., Sachs, T., Schulz, A., Siebert, H., Silva, T., Solomon, A., Sommerfeld, A., Spreen, G., Stephens, M., Stohl, A., Svensson, G., Uin, J., Viegas, J., Voigt, C., von der Gathen, P., Wehner, B., Welker, J. M., Wendisch, M., Werner, M., Xie, Z., and Yue, F.: Overview of the MOSAiC expedition: Atmosphere, Elementa: Science of the Anthropocene, 10, <https://doi.org/10.1525/elementa.2021.00060>, 00060, 2022.
- 740 Si, M., Evoy, E., Yun, J., Xi, Y., Hanna, S. J., Chivulescu, A., Rawlings, K., Veber, D., Platt, A., Kunkel, D., Hoor, P., Sharma, S., Leaitch, W. R., and Bertram, A. K.: Concentrations, composition, and sources of ice-nucleating particles in the Canadian High Arctic during spring 2016, *Atmospheric Chemistry and Physics*, 19, 3007–3024, <https://doi.org/10.5194/acp-19-3007-2019>, 2019.
- Silber, I. and Shupe, M. D.: Insights on sources and formation mechanisms of liquid-bearing clouds over MOSAiC examined from a Lagrangian framework, *Elementa: Science of the Anthropocene*, 10, <https://doi.org/10.1525/elementa.2021.000071>, 2022.
- 750 Solomon, A., de Boer, G., Creamean, J. M., McComiskey, A., Shupe, M. D., Maahn, M., and Cox, C.: The relative impact of cloud condensation nuclei and ice nucleating particle concentrations on phase partitioning in Arctic mixed-phase stratocumulus clouds, *Atmospheric Chemistry and Physics*, 18, 17 047–17 059, <https://doi.org/10.5194/acp-18-17047-2018>, 2018.
- Spreen, G., Kaleschke, L., and Heygster, G.: Sea ice remote sensing using AMSR-E 89-GHz channels, *Journal of Geophysical Research: Oceans*, 113, <https://doi.org/10.1029/2005jc003384>, 2008.
- 755 Stein, A. F., Draxler, R. R., Rolph, G. D., Stunder, B. J. B., Cohen, M. D., and Ngan, F.: NOAA’s HYSPLIT Atmospheric Transport and Dispersion Modeling System, *Bulletin of the American Meteorological Society*, 96, 2059–2077, <https://doi.org/10.1175/BAMS-D-14-00110.1>, 2015.
- Taylor, P. C., Boeke, R. C., Li, Y., and Thompson, D. W. J.: Arctic cloud annual cycle biases in climate models, *Atmospheric Chemistry and Physics*, 19, 8759–8782, <https://doi.org/10.5194/acp-19-8759-2019>, 2019.
- 760 Tian, D., Uieda, L., Leong, W. J., Schlitzer, W., Fröhlich, Y., Grund, M., Jones, M., Toney, L., Yao, J., Magen, Y., Jing-Hui, T., Materna, K., Belem, A., Newton, T., Anant, A., Ziebarth, M., Quinn, J., and Wessel, P.: PyGMT: A Python interface for the Generic Mapping Tools, <https://doi.org/10.5281/ZENODO.8303186>, 2023.
- Tobo, Y., Adachi, K., DeMott, P. J., Hill, T. C. J., Hamilton, D. S., Mahowald, N. M., Nagatsuka, N., Ohata, S., Uetake, J., Kondo, Y., and Koike, M.: Glacially sourced dust as a potentially significant source of ice nucleating particles, *Nature Geoscience*, 12, 253–258, <https://doi.org/10.1038/s41561-019-0314-x>, 2019.
- 765



- Tukiainen, S., O'Connor, E., and Korpinen, A.: CloudnetPy: A Python package for processing cloud remote sensing data, *Journal of Open Source Software*, 5, 2123, <https://doi.org/10.21105/joss.02123>, 2020.
- Vali, G.: Quantitative Evaluation of Experimental Results an the Heterogeneous Freezing Nucleation of Supercooled Liquids, *Journal of the Atmospheric Sciences*, 28, 402–409, [https://doi.org/10.1175/1520-0469\(1971\)028<0402:qeoera>2.0.co;2](https://doi.org/10.1175/1520-0469(1971)028<0402:qeoera>2.0.co;2), 1971.
- 770 Villanueva, D., Stengel, M., Hoose, C., Bruno, O., Jeggle, K., Ansmann, A., and Lohmann, U.: Dust-driven droplet freezing explains cloud-top phase in the northern extratropics, *Science*, 389, 521–525, <https://doi.org/10.1126/science.adt5354>, 2025.
- von Albedyll, L.: Sea ice lead fractions from SAR-derived sea ice divergence in the Transpolar Drift during MOSAiC 2019/2020, <https://doi.org/10.1594/PANGAEA.963671>, 2024.
- von Albedyll, L., Hendricks, S., Hutter, N., Murashkin, D., Kaleschke, L., Willmes, S., Thielke, L., Tian-Kunze, X., Spreen, G., and Haas, C.: Lead fractions from SAR-derived sea ice divergence during MOSAiC, *The Cryosphere*, 18, 1259–1285, <https://doi.org/10.5194/tc-18-1259-2024>, 2024.
- 775 Wegener, A.: Thermodynamik der Atmosphäre, *Nature*, 90, 31–31, <https://doi.org/10.1038/090031a0>, 1912.
- Wehr, T., Kubota, T., Tzeremes, G., Wallace, K., Nakatsuka, H., Ohno, Y., Koopman, R., Rusli, S., Kikuchi, M., Eisinger, M., Tanaka, T., Taga, M., Deghaye, P., Tomita, E., and Bernaerts, D.: The EarthCARE mission – science and system overview, *Atmospheric Measurement Techniques*, 16, 3581–3608, <https://doi.org/10.5194/amt-16-3581-2023>, 2023.
- 780 Wei, J., Wang, Z., Gu, M., Luo, J.-J., and Wang, Y.: An evaluation of the Arctic clouds and surface radiative fluxes in CMIP6 models, *Acta Oceanologica Sinica*, 40, 85–102, <https://doi.org/10.1007/s13131-021-1705-6>, 2021.
- Wex, H., Huang, L., Zhang, W., Hung, H., Traversi, R., Becagli, S., Sheesley, R. J., Moffett, C. E., Barrett, T. E., Bossi, R., Skov, H., Hünerbein, A., Lubitz, J., Löffler, M., Linke, O., Hartmann, M., Herenz, P., and Stratmann, F.: Annual variability of ice-nucleating particle concentrations at different Arctic locations, *Atmospheric Chemistry and Physics*, 19, 5293–5311, <https://doi.org/10.5194/acp-19-5293-2019>, 2019.
- 785 Wieber, C., Jensen, L. Z., Vergeynst, L., Meire, L., Juul-Pedersen, T., Finster, K., and Šantl Temkiv, T.: Terrestrial runoff is an important source of biological ice-nucleating particles in Arctic marine systems, *Atmospheric Chemistry and Physics*, 25, 3327–3346, <https://doi.org/10.5194/acp-25-3327-2025>, 2025.
- 790 Wilson, T. W., Ladino, L. A., Alpert, P. A., Breckels, M. N., Brooks, I. M., Browse, J., Burrows, S. M., Carslaw, K. S., Huffman, J. A., Judd, C., Kilhau, W. P., Mason, R. H., McFiggans, G., Miller, L. A., Nájera, J. J., Polishchuk, E., Rae, S., Schiller, C. L., Si, M., Temprado, J. V., Whale, T. F., Wong, J. P. S., Wurl, O., Yakobi-Hancock, J. D., Abbatt, J. P. D., Aller, J. Y., Bertram, A. K., Knopf, D. A., and Murray, B. J.: A marine biogenic source of atmospheric ice-nucleating particles, *Nature*, 525, 234–238, <https://doi.org/10.1038/nature14986>, 2015.
- Zeppenfeld, S., van Pinxteren, M., Hartmann, M., Bracher, A., Stratmann, F., and Herrmann, H.: Glucose as a Potential Chemical Marker for Ice Nucleating Activity in Arctic Seawater and Melt Pond Samples, *Environmental Science & Technology*, pp. 8747–8756, <https://doi.org/10.1021/acs.est.9b01469>, 2019.
- 795 Zeppenfeld, S., Schaefer, J., Pilz, C., Ebell, K., Zeising, M., Stratmann, F., Siebert, H., Wehner, B., Wietz, M., Bracher, A., and van Pinxteren, M.: Marine Carbohydrates and Other Sea Spray Aerosol Constituents Across Altitudes in the Lower Troposphere of Ny-Ålesund, Svalbard, *EGUsphere*, <https://doi.org/10.5194/egusphere-2025-4336>, 2025.
- 800 Šantl Temkiv, T., Lange, R., Beddows, D., Rauter, U., Pilgaard, S., Dall'Osto, M., Gunde-Cimerman, N., Massling, A., and Wex, H.: Biogenic Sources of Ice Nucleating Particles at the High Arctic Site Villum Research Station, *Environmental Science & Technology*, 53, 10580–10590, <https://doi.org/10.1021/acs.est.9b00991>, 2019.